Assessing the statistical validity of momentum-deficit-based C_D measurements in turbulent configurations

Ander Zarketa-Astigarraga [*], Alain Martin-Mayor, Manex Martinez-Agirre, Markel Peñalba-Retes

Mondragon Unibertsitatea, Faculty of Engineering, Mechanical and Industrial Production, Loramendi 4, Mondragon 20500, Gipuzkoa, Spain

ABSTRACT

An application-agnostic procedure is outlined for checking the validity of momentum-deficit-based drag measurements performed under different turbulent conditions in a wind tunnel. The approach defines a two-step methodology: the first stage characterizes the turbulent flowfield generated downstream a passive grid through a set of statistical parameters. Acceptable values for such parameters are determined by means of two criteria: compliance with the threshold value set by an analysis of the experimental uncertainties, and fulfilment of the isotropic condition for ensuring a well-established turbulent flowfield. Those two prerequisites define a set of turbulent configurations for which the momentum-deficit-based technique applies feasibly.

The second stage of the procedure is configuration-specific, and undertakes drag measurements upon a NACA0021 airfoil subjected to a set of different turbulent configurations. It is shown that performing measurements under invalid turbulent conditions leads to inconsistent drag curves, which serves for defining a validity map based on the testable cases.

1. Introduction

When undertaking aerodynamic design projects, an essential parameter to optimize is the so called aerodynamic efficiency, namely E, defined as the ratio $E = L/D$, where L and D stand for the lift and drag loads that act upon a body immersed in a fluid. The lift load is the one acting perpendicularly to the incoming flow, whereas the drag load lies along the flow's direction and opposes the motion of the body. In an aircraft, L represents the force that sustains the plane in the air; D is the aerodynamic drag that, if unbalanced by the engines' thrust, causes an energy loss on the aircraft that leads to a decrease in velocity and, ultimately, to a decay process coming from the inability of the plane to maintain the required lift value for counteracting its weight. The notion remains valid when considering other applications: the lift load of a wind turbine is directly related to the power output, whereas the drag load decelerates its rotary motion. In both cases, namely the aircraft and the wind turbine, the efficiency factor is an indicator that shows how well the system is behaving from the point of view of an output/input ratio of energies: in the former case, a higher efficiency means that a lower fuel consumption is required for undertaking a flight; in the second one, large E values stand for higher power production rates.

Although measuring lift loads does not usually entail major burdens, direct measurement of drag forces are trickier to perform [1]. Load balances, which are typical devices employed for obtaining lift contributions, can be applied to quantify drags, given the fact that there exist balances allowing to measure forces and momenta along each of the three coordinate axes [2–5]. However, streamlined bodies such as airfoils are characterized by large lift-to-drag ratios under certain flow configurations, with aerodynamic devices like glider planes progressively approaching efficiency values of the order of $E = \mathcal{O}(10^2)$ within a limited range of angles of attack [6]. When a multiaxial balance is used for measuring both lift and drag loads under such circumstances, it is likely that a cross-coupling occurs among its different axes [3]; given the relative smallness of the drag force, such a cross-coupling is liable to affect the resultant value significantly, up to the point of turning the efficiency factor invalid from the standpoint of experimental acceptability. The trade-off solution for measuring drags relies on the so called momentum-deficit method, amply adopted in a number of studies that treat the subject of aerodynamic efficiency [7–14]. Such a method is based on measuring the wake's velocity profile and relating it to the drag exerted upon the airfoil. The decreased velocity observed in the wake region comes from the energy exchange between the airfoil and the flow, an exchange that is caused by mechanisms such as friction processes or pressure differences that are responsible for the drag force [15].

The momentum-deficit method constitutes a well-suited technique for characterizing airfoil-like bodies in wind tunnel configurations. The problem is that such configurations lie far from the ones found in real-world scenarios; wind tunnels are designed for achieving controlled airflow conditions in the test-section, and those conditions may differ greatly from the ones that aircrafts or wind turbines are liable to encounter in their operation environment. When considering applications that operate at low atmospheric levels, such as large- and mid-scale wind turbines or micro aerial vehicles (MAVs) not flying above ≈ 200 m, a relevant factor in their aerodynamic performance is the turbulent intensity present in the environmental flowfield. Close to the ground, the turbulence intensity is reported to be as high as 15%, with such a value depending on the relative velocity of the analysed device and on its operation height [16–19]. Wind tunnels can show turbulence levels that lie far below such values and, in such cases, introducing turbulent effects should constitute a mandatory step in any design process concerned with low-atmospheric-level applications.

Nevertheless, obtaining moderate turbulence intensities does not pose major problems; passive grids are typically employed for reproducing quasi-homogeneous and nearly isotropic flowfields with intensities amply overcoming clean tunnel values [20,21]. Rather, the issue is that the momentum-deficit method is assumed to show certain limitations when applied to turbulent configurations. The studies that employ such a method are not keen on using it in flowfields other than clean wind tunnel ones [7–14], which is an indicative that extending the technique to turbulent configurations is an experimental limitation. This concern has a well-founded rationale behind: whereas delimiting the wake is straightforward in a standard configuration, the presence of turbulent eddies hinders such a task. In the absence of certain parameters assessing that the recorded signal represents a genuine wake profile, the technique itself breaks down. This disables the possibility of measuring the drag coefficient, and the efficiency factor corresponding to a turbulent configuration cannot be obtained. As a result, the design process is not able to account for the overall behaviour of the airfoil in conditions other than the default ones, with the consequences that such a limitation entails.

Apart from the turbulence-related issues, MAV-like devices owning small dimensions and flying at low atmospheric levels show an additional feature: they operate at a flow regime showing Reynolds numbers of Re$\lesssim 5 \times 10^5$. Within the field of aerodynamics, apparatus like commercial aircrafts flying at high subsonic speeds operate at Re $\approx 10^6 - 10^7$, in a regime that is usually considered as fully turbulent. In contrast, the applications addressed herein have a relatively low Reynolds number and fall in an interval known as the transitional regime. In such a regime, both turbulent and laminar features merge, giving rise to complex fluid structures that affect the behaviour of the airfoil by mechanisms not completely understood yet. However, it is a well-established fact that lift and drag values, and hence the aerodynamic efficiency, are highly sensitive to variations in operation conditions such as the level of turbulence or the surface roughness [22–25]. Performing tests on transitionally-operating devices under turbulent conditions has to account for this additional sensitivity in order to achieve meaningful results.

The purpose of the present study is to develop a data-analysis procedure for identifying the conditions under which the momentum-deficit method is applicable to turbulent configurations. The procedure relies on characterizing the turbulent flowfield produced in a wind tunnel by a passive grid [20,21], which is a common technique employed for generating homogenous and isotropic turbulence (HIT hereon) [26,27]. The statistical indicators coming from such a characterization aim at delimiting the spatial interval within the wind tunnel at which HIT conditions hold, and extending the momentum-deficit method to airfoil-like applications operating at turbulent configurations.

The paper is organized as follows: Section 2 lays the fundamentals of statistical analysis, introduces the core notions pertaining HIT and

presents the momentum-deficit method; Section 3 outlines the experimental facility employed for undertaking the tests, and details the configurations that have been surveyed; Section 4 presents the results and discusses the conditions for which the current experimental set-up may be said to comply with the acceptability criteria for undertaking drag measurements in turbulent conditions; finally, Section 5 summarizes the major findings and draws the conclusions that are relevant.

2. Theoretical background

The aim of this section is to lay the fundamentals of the three main topics treated in the work: statistical analysis, experimental turbulence characterization and momentum-deficit method. As said, the necessary mathematical tools for understanding the acceptability criteria derived herein lie on statistics. Such criteria intend to identify and discard the turbulent configurations at which momentum-deficit surveys are not to be performed; the first part of the section verses on such a topic. The second one provides the fundamentals of experimental turbulence characterization by assuming that it develops along the predictions laid by HIT, which is presented briefly. The third part introduces the momentum-deficit method upon which the current drag measurements are based.

2.1. Fundamentals of statistical analysis

Turbulent signals are highly fluctuating and, in order to derive acceptability criteria on the basis of quantifying such fluctuations somehow, it turns necessary to perform a statistical analysis on the data. The set of basic notions required for undertaking the analysis are to be found in the textbook of Olarrea & Cordero [28]. Let $\psi(t)$ be a temporal signal representing a dimensionless, non-deterministic turbulent measurement, and let ϕ be the correspondent random variable that provides the probability distribution function (PDF) of the outcome of such a signal. Mathematically, it is possible to describe the shape of a PDF by a number of scalar parameters that are grouped under the notion of moment; the k-th moment μ_k of a PDF around a specific value μ of the random variable is defined as:

$$\mu_k = \mathrm{E}\left[(\phi - \mu)^k\right], \tag{1}$$

with the operator E$[X]$ denoting the expected value of X [28].

The mean μ of a given distribution corresponds to the centered ($\phi = 0$) first moment ($k = 1$) of a PDF:

$$\mu = \mathrm{E}[(\phi)]. \tag{2}$$

The mean itself does not provide any relevant information beyond identifying the average value of a distribution. However, higher-order moments do: the three statistical indicators of relevance are derived from the second-, third- and fourth-order moments of a distribution, which are named the standard deviation σ, the skewness sk and the kurtosis ku, respectively.

The standard deviation corresponds to the square-root value of the second mean-centered moment, namely:

$$\sigma = \sqrt{\mathrm{E}\left[(\phi - \mu)^2\right]}, \tag{3}$$

and quantifies the scattering of a distribution around its mean; the higher its value, the more scattered the data points are likely to be.

The skewness of a distribution corresponds to its third mean-centered moment:

$$sk = \frac{\mathrm{E}\left[(\phi - \mu)^3\right]}{\left(\mathrm{E}\left[(\phi - \mu)^2\right]\right)^{3/2}}, \tag{4}$$

and it represents a surrogate for the symmetricity of the distribution; the

more positive or negative its resultant value, the higher the amount of data points that lie above or below the average value of the distribution, respectively.

The kurtosis is defined as the fourth mean-centered moment:

$$ku = \frac{\mathrm{E}\left[(\phi - \mu)^4\right]}{\left(\mathrm{E}\left[(\phi - \mu)^2\right]\right)^2}, \tag{5}$$

and highlights the peakedness of a distribution. Taking the probabilities of data points to a fourth power smeares out any quantity lying close to the mean, and the only points that acquire relevant kurtosis values are the outliers of the dataset. Hence, a distribution with a high kurtosis is liable to show a moderate number of data points falling far from the average value.

For illustrative purposes, Fig. 1 depicts three different distributions on its right hand-side diagram. The so called normal distribution is a widely employed gaussian curve in statistical analysis; physical processes with unknown exact distributions are usually assumed to be normal, such as experimental uncertainty propagations, least-square fittings and other applications alike. It is readily observed that a normal curve is symmetric, i.e. $sk = 0$, and it can be shown that has a kurtosis value of $ku = 3$.

A skewed distribution closely resembles a normal curve, but its non-zero skewness value shifts it towards any of the sides around the normal distribution's symmetry axis, depending on the sign of the skewness. In the depicted case such a sign is positive, resulting in the curve tilting rightwards.

A distribution showing a high-kurtosis value is not as similar to the normal curve as the skewed one; instead, it shows a morphology resembling a concave triangle, with the tails falling more slowly for large values of the random variable in contrast to the other distributions. This heavy-tailedness is responsible for the appearance of outliers in the corresponding signal; the fact that large values of the random variable show non-negligible probabilities is the reason for the expected peakedness of such signal.

The left hand-side diagram on Fig. 1 shows the signals derived from the described distributions. The diagram is splitted into three subplots, with the x-axis corresponding to a temporal line and the y-axis representing the dimensionless outcomes coming from the right hand-side distributions. The y-axis is also splitted into three sub-axes, each being normalized to a $[0, 1]$ interval for easing the comparative task. The top signal, coming from the normal distribution and coloured in gray, is reproduced in each of the subplots so that the differences are made apparent. It is observed that in the positively skewed signal the majority of the data points lie above the average value of its normal counterpart,

as described above. The outliers in the high-kurtosis case, represented in the bottom subplot, are also manifest.

2.2. Homogeneous and isotropic turbulence

Homogeneity and isotropy are the two main features ascribed to the turbulent flowfields produced in wind tunnels for experimental testing. A common way for generating an experimental turbulent flowfield is by placing a passive grid at the entrance of the test-section, which acts as localized source of turbulent energy. HIT theory states that, in the abscence of other such sources, the evolution of the turbulent intensity downstream the grid corresponds to a power-law decay of the form [20,27,21]:

$$I = I_0 \left(\frac{x - x_0}{M}\right)^{n/2}. \tag{6}$$

In the above expression, x is a positional argument referring to the streamwise location at which the intensity is measured, and is made dimensionless by the mesh parameter M, which is illustratively defined in Fig. 3. The x_0 variable is the so called virtual origin, and represents the location at which, theoretically, the flow configuration first becomes fully turbulent and begins to comply with the decay laws; n is the exponent that accounts for the power-law expression, and the reason for dividing it by 2 is that, in the formal derivation of the decay laws, the main variable is the turbulent kinetic energy k, which is proportional to the square of the turbulent intensity I. The I_0 prefactor is a scaling variable that may be understood as the intensity value at the streamwise location $x = M + x_0$.

Applying Eq. 6 requires determining the range of the wind tunnel within which such a decay-law holds. It is an accepted fact that the turbulent flowfield downstream a grid is not entirely homogeneous nor isotropic and, instead, it is assumed that quasi-HIT conditions suffice for obtaining turbulent flowfields that evolve following Eq. 6 [29]. Flow homogeneity is addressed by characterizing turbulence along different streamlines and identifying the stage at which the resultant turbulence intensity values merge. In order to acknowledge flow isotropy, Mohsen & LaRue state that the skewness of velocity fluctuations should be null, after an initial period of decay corresponding to non-quasi-HIT turbulent conditions [30]. Accordingly, the approach undertaken herein considers that it is sufficient with showing that the skewness of the streamwise velocity fluctuations remains constant and close to a null value.

With all, delimiting the interval within the wind tunnel for which HIT-like power-law decays hold is a mandatory step before proceeding any further. The experimental procedure employed for characterizing
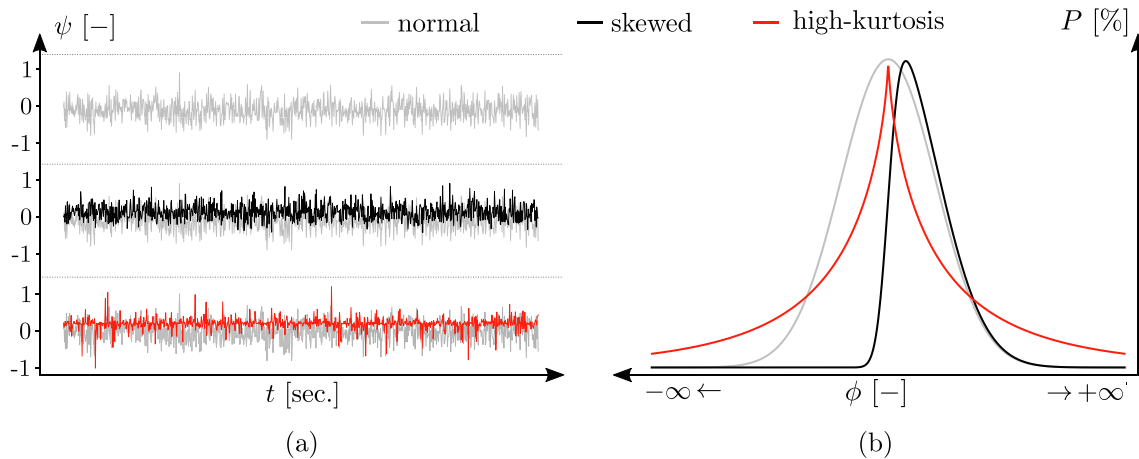

Fig. 1. schematic illustration of (a) three signals coming from a normal, a skewed and a high-kurtosis distributions, from bottom to top respectively, and (b) depictions of the distributions from which those signals are derived. Shared symbols: —— normal distribution; —— skewed distribution; —— high-kurtos.is distribution.

turbulence is outlined in Section 3.

2.3. Fundamentals of momentum-deficit method

The momentum-deficit method is a technique that relies on expressing the aerodynamic drag by combining two of the conservation laws of fluid dynamics, namely the continuity equation and the momentum conservation equation applied along the streamwise direction. The precise derivation of such an expression, which lies out of the scope of the present paper, may be found in the early works of Betz [31], Jones [32] or Bollay [33]. More recently, authors like Takahashi [34], Meseguer & Sanz [1] or Yang & Spedding [7] have treated the subject from a revisionist standpoint, mainly restating the formulation of their predecessors. Notwithstanding the different approaches adopted by the original authors, the conclusion upheld by Takahashi is that the formulations of Betz, Jones and Bollay become equivalent if the wake produced by the airfoil is measured at a sufficiently downstream stage so that the pressure outside the wake recovers its unperturbed upstream value, which occurs for distances of the order of 3 chordwise lengths [34].

If such a condition is met, the momentum-deficit method is relatively simple to apply; the formal derivation that provides the particular expression employed herein may be found in the work of Jones [32] and, more illustratively, in the textbook of Meseguer & Sanz [1]. The derivation itself is performed by applying the conservation laws to a user-set control volume that, in the present case, coincides with a portion of the wind tunnel that encompasses the airfoil. Two of the boundaries of such a volume, which is considered rectangular for the sake of simplicity, are located upstream and downstream the airfoil, and the remaining two are attached to the walls of the wind tunnel.

When an integral formulation of the conservation laws is applied upon such a control volume, it turns possible to link the variables at the downstream boundary to those present in the upstream one. The wall-attached boundaries do not play a role on the final expression, as they provide no contribution to the overall momentum in the streamwise direction. Several assumptions are made regarding the fluid configuration: the flow is assumed incompressible, a condition that is amply fulfilled in a low-Reynolds wind tunnel, as well as two-dimensional, a requisite that is achieved by using endplates for avoiding three-dimensional effects at the tip of the airfoil, as detailed in Section 3.1. The downstream boundary of the control volume is located at such a distance that both the viscous contributions and the unperturbed pressure loss with respect to the upstream boundary are negligible, which allows expressing the drag force thusly:

$$D = \int_w \rho s U_1 (U_0 - U_1) \mathrm{d}w, \tag{7}$$

where D stands for the drag force, s is the spanwise dimension of the airfoil, ρ refers to the density of the fluid and U_0 and U_1 are the streamwise velocity components at the upstream and downstream boundaries, respectively; mind that the integral extends along the entire width of the wind tunnel, namely w.

A convention in aerodynamic studies is to employ dimensionless variables. This is achieved by dividing both sides of the equation by the characteristic load $q_0 \times c \times s$, with $q_0 = \rho_0 U_0^2 / 2$ being the upstream dynamic pressure and c the chord of the airfoil, illustrated in Fig. 4. The U_1 variable represents the velocity profile measured across the width of the tunnel, which means that it is functionally dependent on a cross-sectional parameter, i.e. $U_1 = U_1(y)$. As explained in Section 3, such a curve is measured by a wake-rake device. The wake-rake employed herein does not directly record the velocity of the flow, but the dynamic pressure value proportional to the square of the velocity, i. e. $p_1(y) \propto [U_1(y)]^2$. Naming $y' = y/c$ to the dimensionless y coordinate and changing the dummy variable $w' = w/c$ to y', the momentum-deficit expression adopts the final form:

$$C_D = \int_{y'=0}^{y'=w'} \sqrt{\frac{p_1(y')}{q_0}} \left(1 - \sqrt{\frac{p_1(y')}{q_0}} \right) \mathrm{d}y', \tag{8}$$

where $p_1(y')$ is the pressure curve measured by the wake-rake as a function of the dimensionless coordinate y', and the integral spans between both walls, which are given by the cross-sectional coordinates $y' = 0$ (upper wall in Fig. 4) and $y' = w'$ (lower wall). The experimental procedure for measuring the drag coefficient following Eq. 8 is detailed in Section 3.

3. Experimental set-up

The present section is structured in four different subsections: the first of them describes the physical scenario employed for undertaking the tests, namely the wind tunnel and the set of measurement probes it comprises. The second one introduces the procedure employed for characterizing turbulence, its purpose being to analyse the evolution of the resultant statistical parameters, and not inferring the power-law decays that the turbulent flowfield follows in its downstream evolution. Showing how such laws are derived from the experimental data lies out of the scope of the present work and, instead, the final expressions are provided herein. The third part presents the momentum-deficit-based protocol for undertaking C_D measurements, and has the aim of explaining the particularities of the procedure when applied to the current case. The fourth part is outlines the experimental schedule of the tests and other related issues.

3.1. Physical scenario

As mentioned in Section 1, the aerodynamic devices addressed herein operate at moderately low Reynolds numbers and, accordingly, the experimental set-up for testing them is a low-Reynolds wind tunnel. The set-up itself consists of an open-circuit wind tunnel with a rectangular cross-section of $0.75 \times 1 \text{ m}^2$ and a 3-meters-long test-section. It is a suction type wind tunnel owning a 37 kW fan that is capable of producing flows with peak velocities of 40 m/s in the test-section. The quality parameters of the tunnel, namely its straightness, angularity and background turbulence intensity, are characterized by Torrano providing measured values falling below $0.5\%, 0.5°$ and 0.2%, respectively [25].

A schematic depiction of the experimental set-up, configured for undertaking momentum-deficit surveys, is shown in Fig. 2. The flow comes from a settling chamber placed at the leftmost corner of the figure, and a contraction cone accelerates it so that it enters the test-section complying with the required quality parameters. A *Delta-Ohm HD2001.1* ambient conditions transmitter measures the atmospheric pressure, temperature and relative humidity so that the fluid's density and viscosity are calculated following the humid-air model laid by Picard [35] and Zuckerwar [36]. A *Delta-Ohm HD49047T01L* Pitot-static probe placed at the entrance of the wind tunnel measures the incoming flow's velocity (U). Together with the density (ρ) and viscosity (μ) derived from the ambient transmitter outputs, the chord-based Reynolds number is calculated as Re = $\rho U c / \mu$, which constitutes a dimensionless physical quantity with c standing for the chord of the airfoil. The system allows regulating the tunnel's fan power in order to adjust the velocity, thus achieving control over the Reynolds number. The airfoil, a NACA0021 model having a chordwise dimension of $c = 150$ mm and a span of $s = 900$ mm, is fixed by means of a metallic rod to a rotary plate standing in a sealed box underneath the central panel of the tunnel's floor; such a plate is driven by a remotely controlled *NI ISM 7400* stepper motor, thus achieving an angular degree of freedom around the z-axis of the tunnel that allows controlling the airfoil's angle-of-attack as shown in the cross-sectional illustration placed at the bottom-right region of the figure. The airfoil, placed vertically, is bounded by two endplates located at a pre-established distance from its
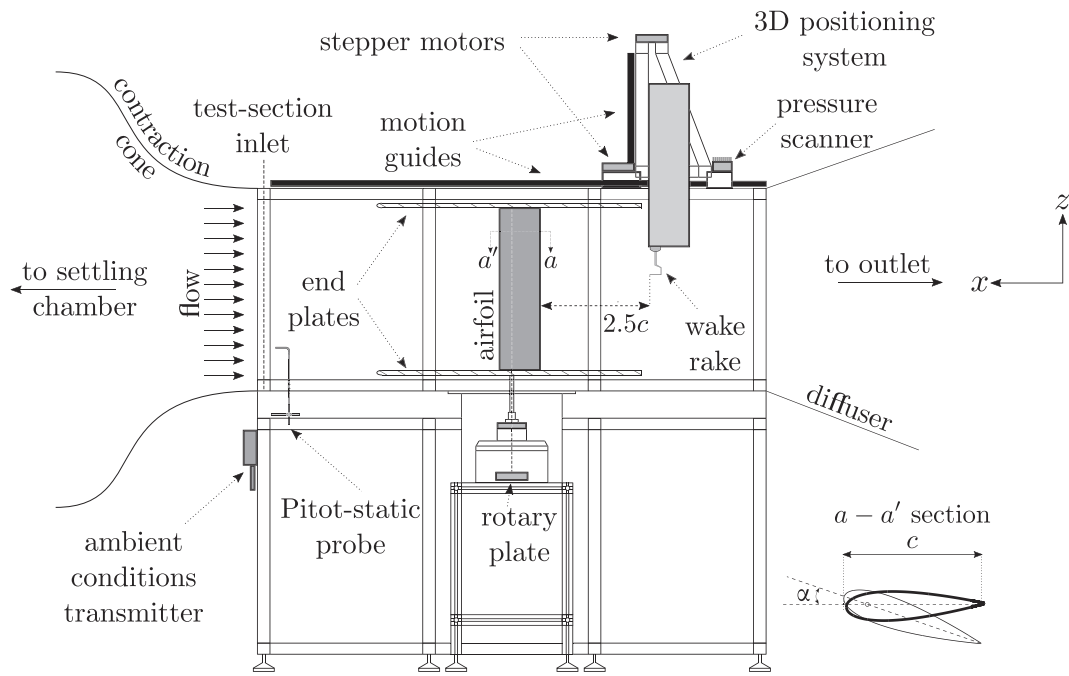
Fig. 2. schematic depiction of the wind tunnel's test-section configured for performing momentum-deficit curve measurements by transversal surveys of the wake-rake device. The settling chamber and the outlet are omitted for the sake of figure compactness. The probes necessary for undertaking the tests are also drafted, as well as the three-axes positioning system required for driving the wake-rake and the rotary plate for tilting the airfoil. The bottom-right sketch represents a cross-sectional plane of the airfoil upon which the angle of attack, α, is defined.

tips for ensuring that three-dimensional effects do not ensue; the airfoil-endplate distance corresponds to a ≈ 2 mm gap according to the estimations made by Torrano [25] following the work of Vaidyanathan et al. [37]. After the test-section, the flow reaches the diffuser stage, where it gets decelerated so that the outlet discharge takes place at a reduced velocity, thus decreasing the pressure gap and augmenting the efficiency of the tunnel.

Between the airfoil and the diffuser, just after the endplates, a holder

having the same NACA geometry as the airfoil is attached to a three-axes positioning system, and enters the tunnel from the ceiling. Such a holder has a drilled hole at its tip for fixing different probes or measurement devices. In the present work, a comb-like wake-rake device designed by *Aerolab* and owning 18 total pressure ports is placed at the tip. When the probe is employed for characterizing turbulence in empty wind tunnel configurations, the endplates and the airfoil are absent from Fig. 2 and the physical scenario resembles the set-up depicted in Fig. 3. In case of
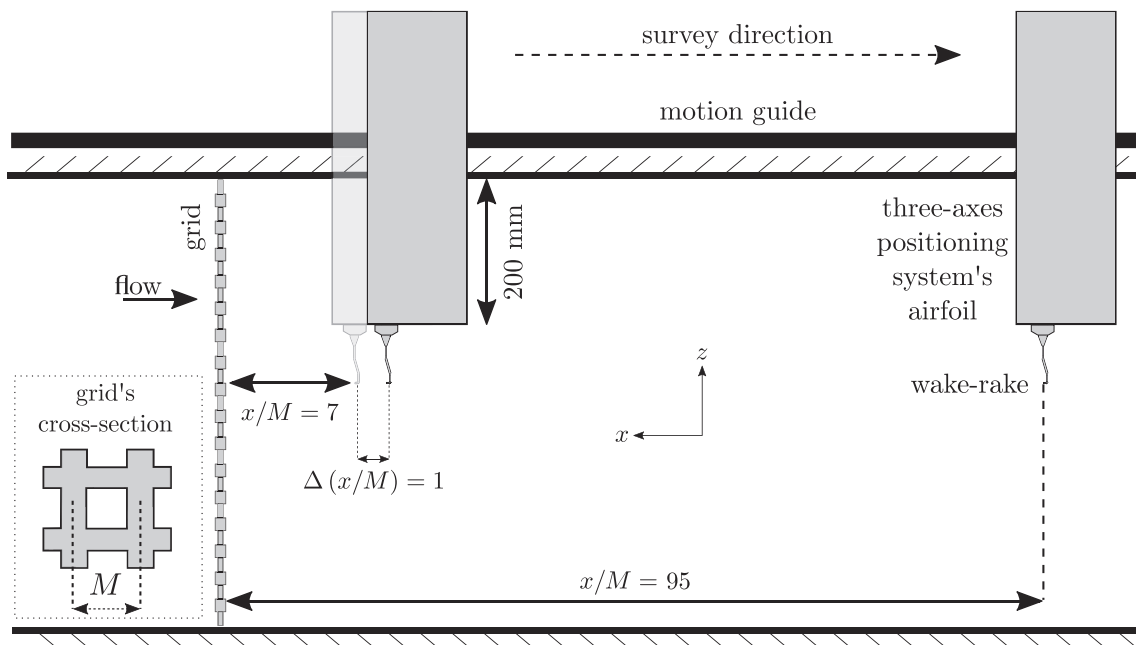

Fig. 3. schematic view of the measurement protocol employed for characterizing turbulent flowfields. The right hand-side view illustrates the cross-section of the employed grid, which has a mesh-spacing parameter of $M = 15$ mm. The probe is placed at an initial dimensionless distance of $x/M = 7$ from the grid, and moved downstream at intervals of $\Delta(x/M) = 1$ until reaching the final stage at $x/M = 95$. At each streamwise stage, a 30-s-long measurement is performed.

wake-rake measurements, the distance between the airfoil's trailing-edge and the wake-rake device is of ≈ 2.5 chord lengths, enough for ensuring that the momentum-deficit method is applied correctly according to the theoretical predictions of Takahashi [34]. The pneumatic lines are taken to a *Scanivalve MPS4264* pressure scanner, a differential device capable of measuring simultaneously from a set of 64 ports at a maximum sampling rate of 850 Hz. The scanner is placed at the top of the wind tunnel, so that the length of the pneumatic lines is reduced in order to avoid compromising the dynamic response of the wake-rake/scanner connection, thus allowing the measurement of turbulence-induced fluctuations. Three independent stepper motors of the type employed for the rotary plate allow moving the three-axes positioning system throughout the tunnel in the streamwise, transversal and vertical directions.

3.2. Reproducing turbulence levels

Intensity levels other than the ones present in clean configurations are achieved by placing a passive rectangular grid upstream the leading-edge of the airfoil. The sudden shear that the flow undergoes when passing through the grid acts as a turbulence production agent. However, no other turbulence sources are placed afterwards and, under such circumstances, the generated intensity level is known to decay according to the mechanisms laid by the HIT theory [26,38]. Although the created flowfield is neither purely homogeneous nor entirely isotropic, the streamwise evolution may be considered to follow the power-law decays prescribed by such a theory with acceptable closeness [21].

For the purposes of the present work, the employed grid consists of a squarely-perforated plate with a mesh-spacing parameter of $M = 15$ mm. Fig. 3 depicts the cross-sectional profile of the grid together with a schematic view of the characterization protocol established by Torrano et al. [39]. Such a protocol is undertaken by placing the wake-rake device at the tip of the holder and positioning it at an established dimensionless distance from the grid, namely $x/M = 7$, as approaching the probe closer to the grid causes spurious effects on the signals. Once the tunnel is operating at the target Reynolds number, a 30-seconds-long measurement is performed, which is considered a large enough lapse for undertaking a proper statistical analysis [39]. Afterwards, the holder is moved downstream a distance of $\Delta(x/M) = 1$, the flow-device system is left to establish for a period of 5 seconds, and the next 30-seconds-long measurement is registered. This motion-halt-acquisition cycle is repeated until the dimensionless streamwise stage $x/M = 95$ is reached. A LabVIEW application [40] monitores the system in real time, automating both the data-acquisition and the probe-motion operations. Homogeneity is ensured, first of all, by noticing that the 18 wake-rake ports provide quantitatively matching statistical parameters, which indicates that the flow is homogeneous in the transversal direction. Second of all, tests run at different positions show that the same occurs in the vertical direction.

The described protocol results in a set of streamwise temporal signals that allow characterizing the evolution of the turbulent flowfield downstream the grid. Passive-grid-induced turbulence is known to develop a non-isotropic, heterogeneous region that extends a short distance downstream the grid, becomes a quasi-HIT flowfield afterwards and undergoes a final decay process at the farfield zone, which also deviates from the expected HIT behaviour [41]. Establishing such zones, which ultimately delimit a spatial region of the wind tunnel within which the power-law decays are valid, is a proper task of the characterization process. Such a process is analysed in terms of the statistical parameters described in Section 2.1, with the aim of showing the effects of performing wake-rake measurements at streamwise positions that lie outside the quasi-HIT region; for the sake of conciseness, the power-law decay of the turbulent intensity parameter is provided without further specifications, merely mentioning that it is obtained from the set of measurements performed within the quasi-HIT region by means of the "maximum decay range" method presented by Krogstad & Davidson

[21]. Such a decay follows the expression:

$$I = 28.5 \left(\frac{x}{M} - 5 \right)^{-0.58}, \tag{9}$$

valid within the range of Reynolds numbers for which the tests are to be undertaken. Those values lie acceptably close to the ones found in similar studies treating the subject of grid-generated turbulence [21,42]. Knowing that the decay laws are universal, such a matching is to be understood as a cross-check proof for the current characterization.

3.3. C_D measurement protocol

The two-dimensional cross-section depicted in Fig. 4 intends to show a generic $x - y$ plane in order to understand how the momentum-deficit method is applied. As mentioned in Section 2.3, the technique consists of measuring the velocity profile of the wake and integrating it afterwards for getting the correspondent C_D value. In order to capture the wake adequately, the wake-rake's transversal survey needs to be extended until the unperturbed flow region at both sides of the deficit curve. When testing airfoils that operate in the transitional regime, it is a sensible practice to obtain efficiency values for angular configurations that go beyond the stalling condition of the airfoil. Stalling occurs when the flow is not able to overcome the adverse pressure gradient imposed by the geometry of the airfoil at moderate angles-of-attack and, consequently, it detaches from the surface turning the airfoil into a bluff-body. In contrast to its streamlined-body behaviour, the efficiency of a stalled airfoil undergoes a sharp decrease, and the angle-of-attack needs to be lowered in order to recover unstalled conditions. However, unstalled conditions are not usually recovered when decreasing the angle-of-attack below that for which the airfoil stalls, but for a distinct angular configuration of a lower value; this behaviour, known as aerodynamic hysteresis, is reported to vary with flow conditions such as the Reynolds number or the turbulence intensity [25], and its assessment is a major step of the designing process. That's why the surveys undertaken herein measure the drag coefficient for a set of angles-of-attack spanning the range $\alpha \in [0, 20]°$ with $\Delta \alpha = 1°$; the upper bound of $20°$ is set by observing, experimentally, that the airfoil stalls at an angle-of-attack that lies close to such a value. Afterwards, and in order to account for the hysteretic behaviour, the airfoil is rotated back to its starting position following the inverse route, i.e. $\alpha \in [20, 0]$ with $\Delta \alpha = -1°$.

Let Fig. 5 illustrate how a C_D value is obtained for a given angular configuration of the airfoil. The plotted datasets correspond to wake-rake measurements undertaken for a case in which the airfoil is fixed at its $0°$ configuration. The x-axis of the plot represents the non-dimensional wake-rake position, $y' = y/c$, with y being the transversal distance measured from the trailing-edge of the airfoil when it is fixed at an angle-of-attack of $0°$. Considering, by empirical observation, that the wake can be as wide as two chordwise dimensions when the airfoil is stalled, and that the wake-rake device spans approximately a third of the chord's value, it turns necessary to perform a set of measurements for covering the wake entirely in the overall set of angular configurations. For that purpose, the transversal section is divided into seven portions having the same length as the wake-rake; the central portion is located behind the airfoil's trailing-edge when it is oriented in its $0°$ configuration, and the rest of the zones are located a distance of $c/3$ away from each other starting from the central portion and filling the transversal dimension of the wind tunnel in both directions. Thus, the total length covered by the set of seven measurements is of $7c/3 > 2c$, which suffices for measuring the wake adequately. The spaces between the dotted vertical lines that split the x-axis have the length of the wake-rake device, so that the points enclosed within any such pairs of lines correspond to one of the seven measurements performed when obtaining the curve. The triangular and circular symbols stand for the raw and filtered datasets respectively, and the bell-like curve outlining the shape of the momentum-deficit profile is a gaussian approximation that helps
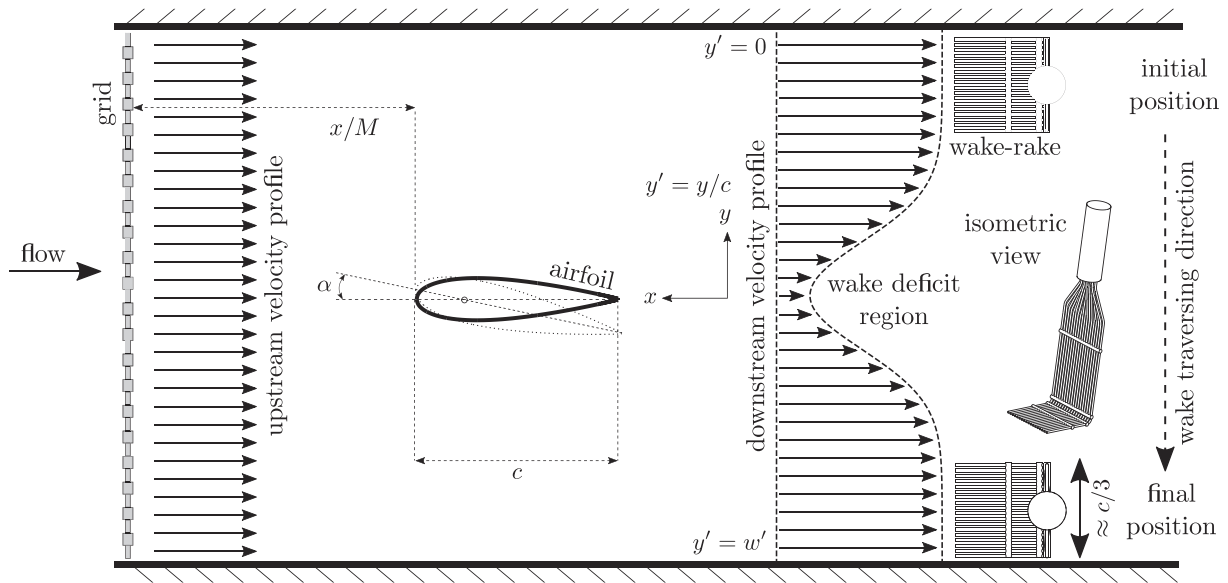
Fig. 4. schematic depiction of the momentum-deficit curve measurement by wake-rake survey. The wake-rake is shown for illustrating that the transversal survey begins from the $y' = 0$ position and finishes at the $y' = w'$ one. The difference between the upstream and downstream velocity profiles is made apparent so that the wake deficit region gets represented. The passive grid located upstream the leading-edge of the airfoil generates a turbulent flowfield downstream of it.
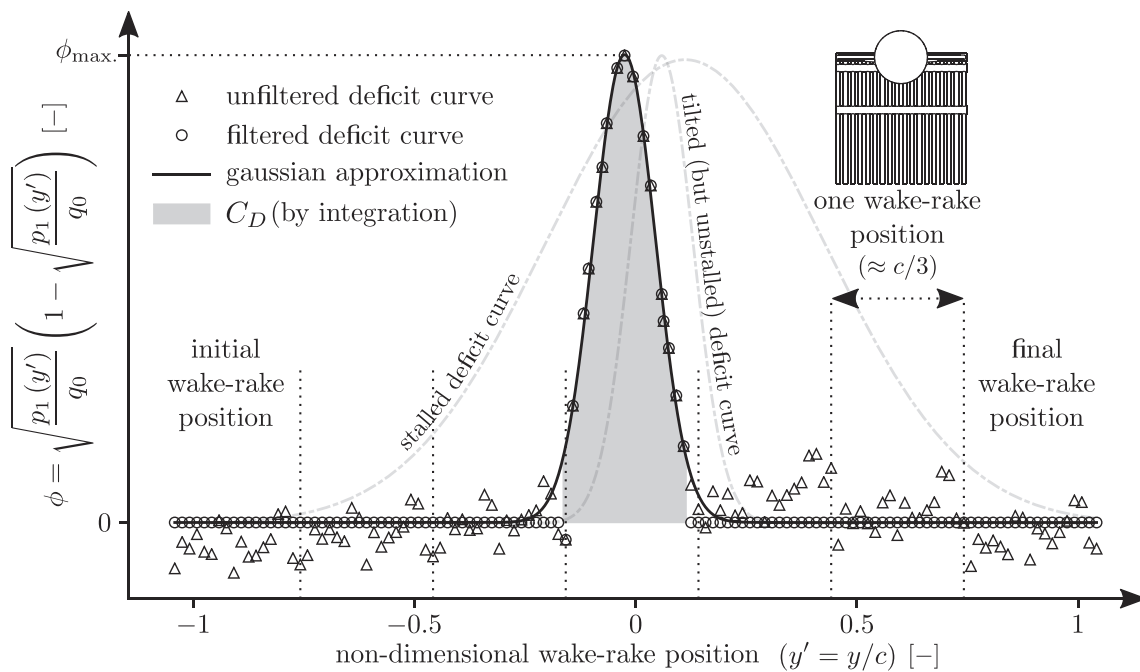

Fig. 5. representation of a momentum-deficit curve obtained for a given angular configuration of the airfoil. The x-axis stands for the non-dimensional wake-rake position; the upper-right sketch corresponds to a top view of the wake-rake device. The y-axis represents the momentum-deficit magnitude. △: unfiltered deficit curve; ◯: filtered deficit curve; ——— gaussian approximation of the filtered momentum-deficit curve; ▨ area corresponding to the C_D value; –·–·– momentum-deficit curves corresponding to other angular. configurations.

visualizing the plot, as it allows shading the area that corresponds to the C_D value; the filtering process is thoroughly explained in the work of Zarketa-Astigarraga et al. [43]. When changing the angle-of-attack of the airfoil, the wake is liable to shift its position sideways, depending on how the new angular configuration affects the flowfield; likewise, the plotted curve corresponds to an unstalled airfoil configuration, with the spanwise length of the wake not exceeding half of the chord's length, i. e. $\ell_{\text{wake}} \approx c/2 = 75$ mm. The dashed-dotted lines represent, on the one hand, how the momentum-deficit curve tilts when changing the angle-of-attack and, on the other hand, how it widens when stalling occurs.

Thus, the protocol for measuring a $C_D - \alpha$ curve starts by setting the tunnel at a predefined Reynolds number and fixing the airfoil at its $0°$ angular configuration. Afterwards, the wake-rake is moved to the left-most position of the wind tunnel's y-axis, which is where the transversal survey begins. The flow is left to stabilize for two seconds before making a 5-s-long measurement, and the wake-rake is moved rightwards to the next position, where the stabilization-measurement combination is repeated. When the wake-rake reaches its rightmost position and the measurements for the current momentum-deficit curve are completed, the airfoil is rotated to its next angular configuration and the wake-rake

displaced to its initial position, starting the transversal survey again. As for the turbulence characterization protocol, the automatization of the data-acquisition process is achieved via a LabVIEW program.

3.4. Experimental schedule and related issues

The overall experimental schedule consists of two main parts; the first of them deals with the turbulence characterization as described in Section 3.2, and the second one addresses the momentum-deficit-based C_D measurements in compliance with the protocol presented in Section 3.3.

Turbulence characterization protocols are undertaken for a set of four different Reynolds numbers, namely $\mathrm{Re} = \{0.6, 0.8, 1, 1.2\} \times 10^5$, for which the momentum-deficit-based C_D measurements are performed. Each of those four cases yields a dataset comprising 87 wake-rake measurements that represent the streamwise evolution of the corresponding turbulent flowfields.

Regarding the C_D-related aspect, the experimental schedule shown in Table 1 is designed for assessing the statistical validity of momentum-deficit-based measurements in different turbulent configurations, considering the effects induced by the two main flow-related parameters, namely the Reynolds number and the turbulent intensity level.

The angular route described above allows capturing the hysteresis cycle and forcing the airfoil to stall, and is the same regardless the configuration being tested. Four different case-studies are defined for the clean wind tunnel configuration, with the Reynolds number varying in the range $\mathrm{Re} \in [0.6, 1.2] \times 10^5$ at intervals of $\Delta \mathrm{Re} = 0.2 \times 10^5$; these variations aim at acknowledging that the momentum-deficit method remains statistically acceptable within the mentioned Reynolds interval if the clean configuration is kept. The turbulent configurations follow a logic that will become clear further on, after presenting the results concerning the turbulent characterization process.

The upper and lower bounds for both parameters are chosen on the basis of the physical constraints imposed by the wind tunnel system. Regarding the Reynolds number, the flow turns unstable when the fan's rotation becomes exceedingly slow, and a lower bound of $\mathrm{Re} = 0.6 \times 10^5$ is observed to be sensible enough for avoiding such an instability; as for the upper bound of $\mathrm{Re} = 1.2 \times 10^5$, the blockage introduced by the passive grid does not allow increasing the Reynolds number further due to the power limitation of the fan. When considering the turbulence intensity parameter, Eq. 9 shows that higher levels are achieved when placing the grid closer to the leading-edge of the airfoil; the nearest position is constrained due to the presence of the endplates, and corresponds to a dimensionless leading-edge distance of $(x - x_0)/M = 32$. The grid needs to be placed downstream the Pitot-static probe, which yields a maximum distance of $(x - x_0)/M = 56$. Following Eq. 9, those distances corrspond to turbulence intensity levels of 3.8% and 2.75%, respectively.

Each configuration is tested thrice for the sake of repeatability, with every dataset undergoing a post-processing routine by which the experimental uncertainty intervals of the measured magnitudes are computed as prescribed in the work of Zarketa-Astigarraga et al. [43].

As shown in Section 4, having the uncertainty intervals is relevant insofar they provide a straightforward parameter for defining acceptability criteria. Those intervals are calculated by setting a confidence level of 95% on the probability of finding an outlier on a given dataset, which means that the outcome of a measurement shows a 5% chance of yielding a magnitude that differs from its average value more than the quantity prescribed by the uncertainty interval. As the intervals are obtained from the standard deviations of the measurement signals [44], the uncertainty analysis and the statistical parameters laid in Section 2.1 are directly related. Exploiting such a relation is essential for assessing the validity of a momentum-deficit-based C_D measurement undertaken in a turbulent flow configuration.

Nevertheless, Section 1 has already mentioned the high sensitivity of transitionally-operating airfoils to flow conditions and geometrical features, and such a sensitivity affects the choice of the confidence level by which the uncertainty intervals are obtained. In a transitional regime, phenomena like flow separation and reattachment are highly unstable, with airfoil drag values depending non-linearly on the input parameters like the angle-of-attack or the Reynolds number [8,45]. In fact, Ol et al. show that airfoil tests undertaken in nominally equivalent conditions, but at different experimental set-ups, yield discrepancies higher than 20% on the location and extent of transitional aerodynamic structures, meaning that differences in drag values larger than 5% are to be expected when comparing results among different studies [46]. Likewise, Guglielmo & Selig show the predominance of such unstable structures below $\mathrm{Re} = 10^5$ and the inherently large uncertainty intervals that are ascribed to C_D values [47]. These facts can make the choice of the 95% confidence level look exceedingly restrictive, as larger errors may be acceptable according to the literature. In spite of it, there are two reasons for adopting such a confidence level: the first one is that, unlike in the study of Ol et al., the present approach does not intend to perform inter-facility comparisons, but to characterize the validity of a measurement technique in a specific wind tunnel. The second reason is that achieving controlled conditions in a set-up with a 95% confidence level is a common assumption in experimentalism [48–50], as it constitutes a trade-off between the need of assuming errors in measurements and avoiding that an excessively large amount of outliers are considered as valid data-points, which would compromise the quality and relevance of the results. The same confidence level is employed in the work of Zarketa-Astigarraga et al. for obtaining the uncertainty intervals of the basic measurands that determine the operation conditions of the wind tunnel [43].

4. Results and discussion

The dataflow of results is organized following the same structure as in Section 3: the streamwise evolutions of the statistical parameters corresponding to the characterization of turbulent flowfields are presented first, together with a discussion that establishes the acceptability criteria for undertaking momentum-deficit tests in turbulent configurations. Next, it is shown that violating such acceptability criteria leads to invalid $C_D - \alpha$ curves. Finally, a $\mathrm{Re} - I$ validity map is provided, delimiting the regions within which momentum-deficit-based C_D measurements are safely reproducible.

4.1. Turbulence characterization

Let Fig. 6 describe the streamwise evolution of the standard deviation of turbulent velocity fluctuations, namely σ. For the sake of conciseness, Figs. 6–8 share the same x-axis, whereas the y-axes represent the statistical parameter that corresponds to each figure; the magnitudes of both axes are dimensionless. The dashed vertical lines on the right hand-side of the figures represent the streamwise distances between the wake-rake (where the C_D measurements are made) and the grid required for obtaining specific turbulent intensity values at the leading-edge of the airfoil, namely $I = \{2.75, 3, 3.8\}\%$.
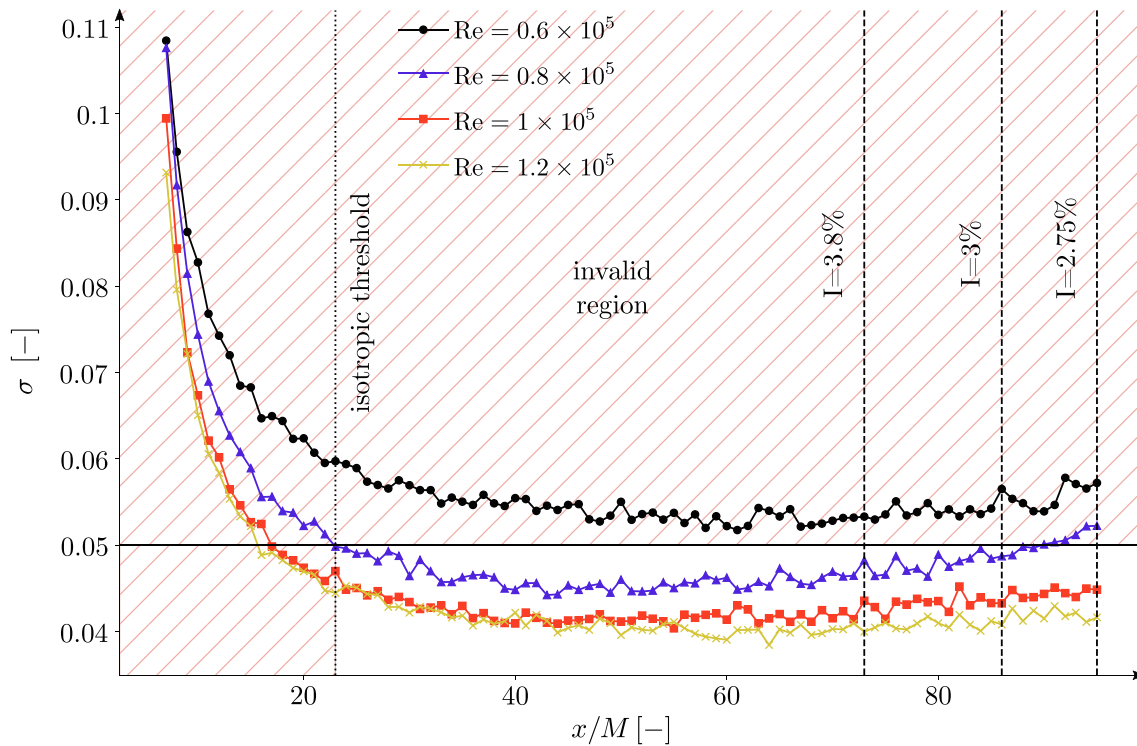
Table 1
parametrical schedule for the experimental testing campaign.

	cChord-based Reynolds number [−]	Turbulence intensity [%]	Angular route [°]
Clean configurations	$\mathrm{Re} \in [0.6, 1.2] \times 10^5 \Delta(\mathrm{Re}) = 0.2 \times 10^5$	0.2%	$\alpha \in [0, 20]$ $\Delta\alpha = 1$ ∪ $\alpha \in [20, 0]$ $\Delta\alpha = -1$
Turbulent configurations	0.6×10^5	3.8	
	0.8×10^5	$\{2.75, 3.0, 3.8\}$	
	1×10^5	2.75	
	1.2×10^5	2.75	

Fig. 6. streamwise evolution of the standard deviation of turbulent velocity fluctuations, σ. ⚫—⚫: Re $= 0.6 \times 10^5$; ▲—▲: Re $= 0.8 \times 10^5$; ■—■: Re $= 1 \times 10^5$; ✕—✕: Re $= 1.2 \times 10^5$. The x-axis stands for the dimensionless streamwise distance, x/M, and the y-axis represents the standard deviation of velocity fluctuations, σ.

As Fig. 6 shows, larger Reynolds numbers induce lower standard deviations along the streamwise dimension. This means that the oscillations perceived by the wake-rake probe are less scattered around their mean value, in accordance to the definition of the σ parameter. The streamwise positions at $x/M \lesssim 20$ constitute an initial region of rapid decay, showing that near the grid the measured signals are highly fluctuating. Such streamwise positions correspond to the non-homogeneous, anisotropic region described by Djenidi et al. [41] and, for that reason, it is considered an invalid zone for undertaking turbulent measurements. Downstream $x/M \approx 20$ the evolution of the curves becomes milder, with the velocity fluctuations showing relatively smaller values of σ. The analysis undertaken by Zarketa-Astigarraga et al. [43] relates the uncertainty intervals of the measured quantitites to their standard deviations, which allows delimiting the region for which the turbulent measurements are valid; in fact, the statistical confidence level employed for deriving such intervals is of $\alpha|_{\text{conf.}} = 0.95$ [43]. A way of interpreting such a confidence level is to assume that signals owning standard deviations larger than $1 - \alpha|_{\text{conf.}} = 0.05$ fall outside the validity range of experimental acceptance. In Fig. 6, this condition is represented by the solid horizontal line, with the region above it being as invalid as the initial zone. Hence, a curve becomes a potential measurement candidate whenever it falls below the mentioned conditional line; it is readily observed that the Re $= 0.6 \times 10^5$ case does not fulfill such an acceptability condition for any of the streamwise positions. The dotted vertical line at the left hand-side of the figure represents a conservative boundary of the valid region, as it is traced at the first x/M position for which the three remaining cases are experimentally valid. The reason for naming it as "isotropic threshold" is given further on.

The analysis above shows that the valid region for undertaking turbulent measurements lies below the $\sigma = 0.05$ threshold and extends between $x/M \in [23, 95]$. Such a region plays an essential role when calculating the power-law decay of the turbulent intensity by means of the "maximum decay range" method presented by Krogstad & Davidson [21]. Indeed, if the values in Eq. 9 are observed to match those obtained

by Krogstad & Davidson is due to the fact that the points employed for deriving the decay law lie within such a region. Any of the Re $= \{0.8, 1, 1.2\} \times 10^5$ cases yields similar values of the decay law parameters, and the three of them deviate comparably from the expected theoretical values when including points that correspond to the initial non-homogeneous, anisotropic region. Additionally, the Re $= 0.6 \times 10^5$ case does not provide acceptable decay law parameters, which is expectable given its experimental invalidity. Two additional comments are necessary: the first is that there are certain points of the Re $= \{1, 1.2\} \times 10^5$ cases that, although lying below the conditional line, stand within the invalid initial region. Technically, such points represent valid candidates for deriving power-law decays or performing momentum-deficit-based C_D measurements, because the isotropic threshold is case-specific, with each curve owning its particular line. However, the line on Fig. 6–8 is plotted following a conservative approach, and marks the first streamwise position for which the three curves become experimentally valid. The second remark has to do with the behaviour of the Re $= 0.8 \times 10^5$ case at the most downstream locations. For $x/M > 90$, the curve lies above the conditional line; thus, the Re $= 0.8 \times 10^5$ case produces a turbulent flowfield that is not momentum-deficit-measurable at $I = 2.75\%$.

So far, the σ-based acceptability criterion allows discarding certain turbulent configurations in advance; concretely, C_D measurements become unfeasible for the three turbulent intensity values at Re $= 0.6 \times 10^5$, as well as for the $I = 2.75\%$ value at Re $= 0.8 \times 10^5$. The σ-based criterion, thus, is logically sufficient for ensuring the validity of turbulent configurations. A straightforward question arises: is it also necessary? Is any configuration complying with the σ-based criterion momentum-deficit-measurable? For answering such a question, consider the streamwise evolutions of the skewness parameter depicted on Fig. 7. The datasets show a large scattering, with the standard deviation of the skewness values ranging between $\sigma(sk) \in [3.66, 5.23] \cdot 10^{-2}$, with those limits corresponding to Re $= \{1.2, 0.6\} \times 10^5$ numbers, respectively. Such a scattering is an order of magnitude higher than the
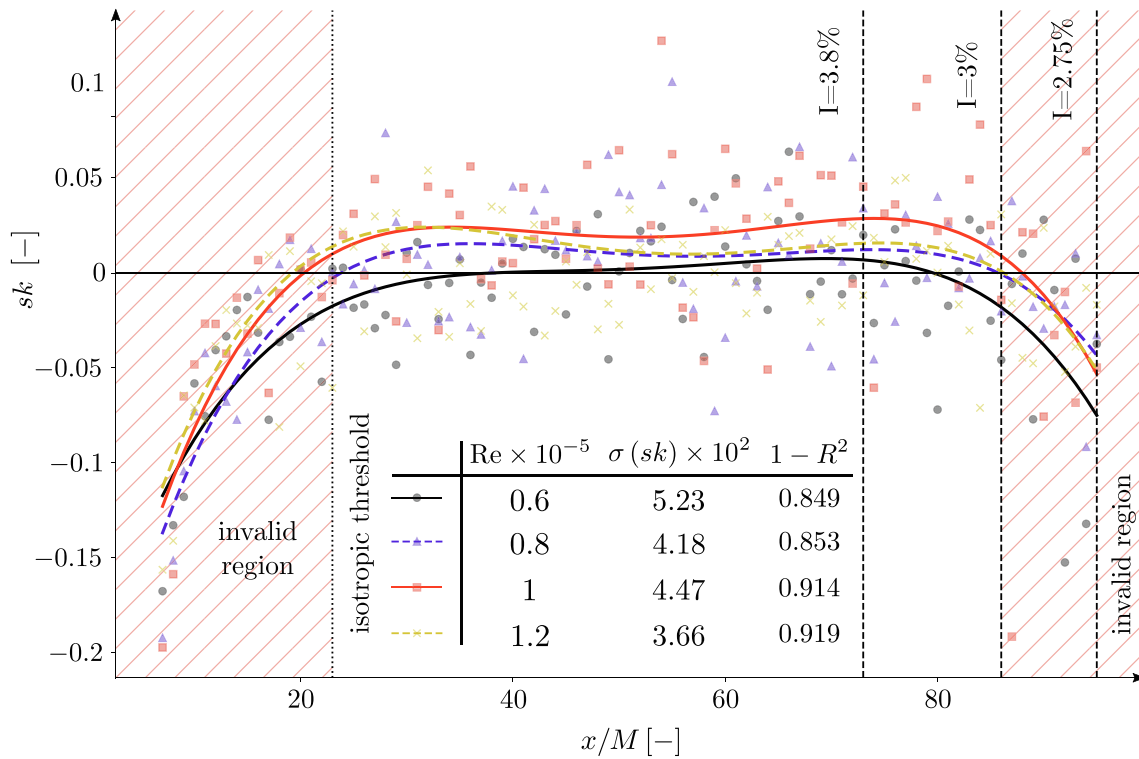
Fig. 7. streamwise evolution of the skewness of turbulent velocity fluctuations, *sk*. ⟶●⟶: Re $= 0.6 \times 10^5$; - - -▲- - -: Re $= 0.8 \times 10^5$; ⟶■⟶: Re $= 1 \times 10^5$; - - -✕- - -: Re $= 1.2 \times 10^5$. The *x*-axis stands for the dimensionless streamwise distnace, x/M, and the *y*-axis represents the skewness of velocity fluctuations, *sk*.

largest values observed in Fig. 6, which is an additional indicative of the fluctuating nature of the signals. In order to ease the understanding of the measured trends, the datasets are approximated by polynomial fits that are plotted as solid lines, with the goodness of the fits extending between $1 - R^2 \in [0.91, 0.85]$ (R being the residual of the polynomial fitting) and complying with the same Reynolds number order as for the $\sigma(sk)$ parameter. Thus, higher Reynolds numbers induce a slightly lower scattering, resulting in a marginally better fitting of the polynomial curves. According to the analysis of Mohsen & LaRue [30], a grid-generated turbulent flowfield may be assumed to become locally isotropic when the velocity skewness is null. Such a criterion is interpreted here by considering that a nearly constant, close-to-zero value is sufficient for claiming that isotropic conditions ensue. Thus, the central region of the figure at which the fittings become flat is isotropic and, as the flowfield is homogeneous according to Section 3.2, quasi-HIT conditions are fulfilled.

The fittings become approximately flat for $x/M \gtrsim 20$. On this respect, the σ-based criterion matches the *sk*-related analysis, and both predict the same streamwise location beyond which the flowfield becomes experimentally acceptable (σ-based analysis) and statistically isotropic (*sk*-related analysis). It is doubly asserted, hence, that the task of obtaining the power-law decays must avoid the initial region of non-homogeneous, anisotropic turbulence. However, the most downstream positions also show a marked tendency to deviate from the expected quasi-flat behaviour, a fact that occurs regardless of the considered Reynolds number. Although it is found that neglecting such points does not modify the parameters of the power-law decays, they may pose an additional constraint on the feasibility of momentum-deficit-based C_D measurements. Although violating the σ-based criterion is sufficient for discarding a given turbulent configuration, fulfilling it may not be necessary for stating that such a configuration is momentum-deficit-measurable, given the analysis of Fig. 7. It turns necessary to analyse the $C_D - \alpha$ curves that comply with the σ-based criterion, namely Re $= \{1, 1.2\} \times 10^5$, at turbulent intensities for which the *sk* analysis predicts

anisotropic behaviour, i.e. $I = 2.75\%$. If such curves are spurious in some sense, then the σ-based criterion must be complemented with additional postulates for ensuring the momentum-deficit-measurability.

Lastly, consider the streamwise evolutions of the kurtosis parameter shown in Fig. 8. The points of the different datasets lie close to the gaussian value of 3 for the major part of the curve. In contrast to the σ and *sk* parameters, the kurtosis seems unaffected by the initially non-homogeneous, anisotropic region. The only explanation is that, according to the theoretical definition of *ku*, the outliers of the signals do not become relevant at such an initial stage, which stands at a highly scattered (large σ) and largely skewed (negative *sk*) region of the flowfield, albeit with quantitatively small deviations from the mean (low *ku*). However, there does not seem to be a *ku*-based criterion for delimiting such an initial region, unlike for the σ and *sk* cases. Given that those two parameters provide the same threshold, it is assumed that the behaviour of *ku* at the most upstream positions does not refute the fact that there exists an invalid initial zone. Rather, such a behaviour is an indicative of the inadequacy of the kurtosis parameter for detecting the anisotropic nature of the flowfield in the nearfield of the grid. Thus, such a nearfield is not tagged as invalid on the figure, although the isotropic threshold is drawn as in Figs. 6 and 7 for the sake of coherence.

On the other hand, Fig. 8 does seem to highlight the problems that may arise when trying to undertake momentum-deficit-measurements at the most downstream positions. The kurtosis parameter increases suddenly beyond $x/M = 86$ (the stage for which a turbulent intensity of $I = 3\%$ is obtained at the leading-edge of the airfoil). It looks like the kurtosis parameter partially complements the *sk*-based analysis, in the sense of highlighting the need for checking how the $C_D - \alpha$ curves of the σ-criterion-compliant cases, namely Re $= \{1, 1.2\} \times 10^5$, behave at $I = 2.75\%$. The conclusion drawn from the analysis of either of these parameters is straightforward: that a single, σ-based acceptability criterion may not be sufficient for identifying the overall set of invalid configurations. The aim of the following section is to analyse the $C_D - \alpha$ curves for determining whether such an implication is sound.
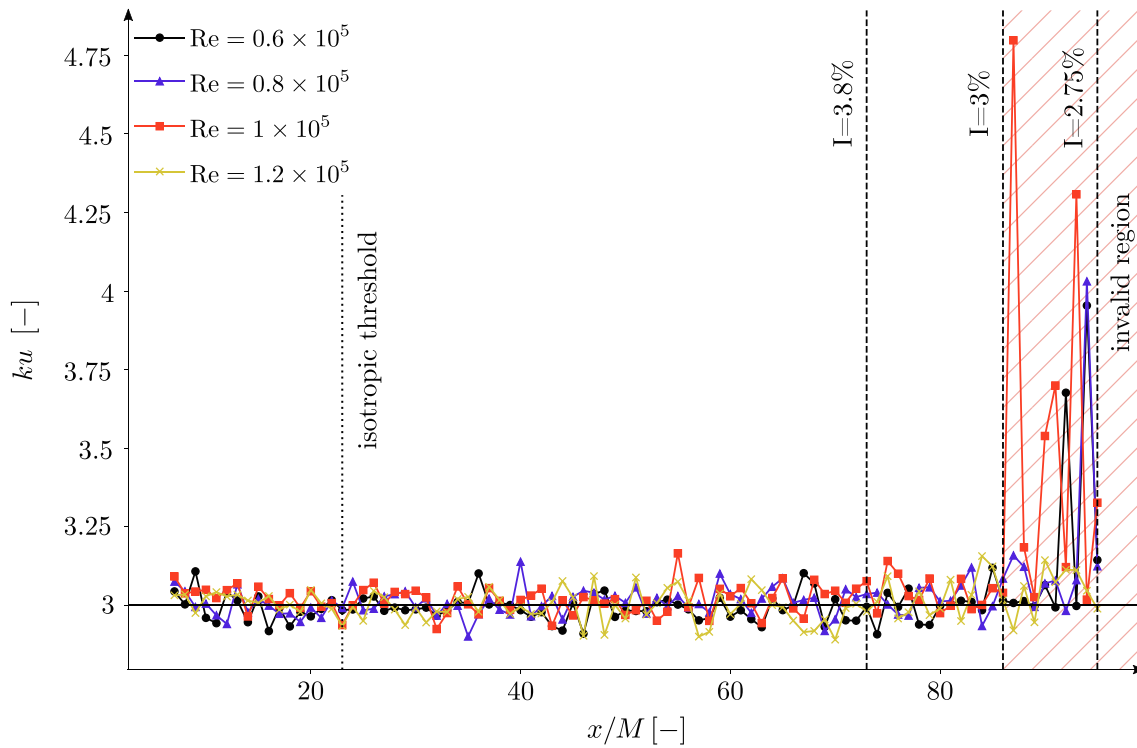
Fig. 8. streamwise evolution of the kurtosis of turbulent velocity fluctuations, ku. ——●——: Re $= 0.6 \times 10^5$; ——▲——: Re $= 0.8 \times 10^5$; ——■——: Re $= 1 \times 10^5$; ——✕——: Re $= 1.2. \times 10^5$.

4.2. Effects on $C_D - \alpha$ curves

As mentioned in Section 3.4, the logic of the experimental schedule shown in Table 1 becomes clear on the light of the results provided by the turbulence characterization process. Such a table represents the different configurations for which a $C_D - \alpha$ curve is obtained by means of the momentum-deficit method. The ones on the first row correspond to clean configurations tested at the same Reynolds numbers as those for which the turbulent characterization process has been undertaken; the aim of such configurations is to show that, in the absence of grid-generated turbulence, the momentum-deficit method remains valid regardless of the considered Reynolds number.

The turbulent configurations are chosen so that they reproduce a set of significant cases from the standpoint of experimental validity. The first case intends to confirm that the lowest Reynolds number provides invalid $C_D - \alpha$ curves regardless of the introduced turbulence intensity level; the fact of choosing the $I = 3.8\%$ case is that, according to Fig. 7, the flowfield is still within a locally isotropic region at such a streamwise position. If the resultant $C_D - \alpha$ curve is invalid, it means that violating the σ-based criterion is sufficient for discarding a given configuration.

The three turbulent cases at Re $= 0.8 \times 10^5$ aim at corroborating the mentioned condition, as two of them ($I = \{3, 3.8\}\%$) are σ-compliant, whereas the one at the lowest turbulence intensity level is not. However, the σ-compliant ones also remain within the isotropic region depicted on Fig. 7, so they cannot determine whether fulfilling the σ-based condition is a necessary prerequisite for ensuring the experimental validity of the curves. This condition is checked by the Re $= \{1, 1.2\} \times 10^5, I = 2.75\%$ cases, which are the ones standing outside the isotropic region, but showing standard deviations that lie below the critical threshold value. In case they provide invalid $C_D - \alpha$ curves, it is to deduce that ensuring isotropy is equally relevant as complying with acceptable σ values.

Once the logic of the tested configurations is well established, a further question remains: what counts as a valid $C_D - \alpha$ curve? Defining a proper notion of validity seems necessary in order to distinguish between genuine and spurious configurations. For that purpose, the shape

of the $C_D - \alpha$ curves are analysed by following the angular route described in Table 1. Fig. 9 shows two of such curves, one that corresponds to a valid, clean configuration tested at Re $= 0.8 \times 10^5$ and the other to an invalid turbulent case; the x-axis represents the angle-of-attack α, and the y-axis stands for the drag coefficient C_D. The plotted lines represent the average of three different curves obtained for each configuration in order to ensure repeatibility, as mentioned in Section 3.4.

There are two features on the figure that are worth mentioning. The first is that the hysteretic behaviour of the airfoil gets clearly reflected on the plots. Consider the dataset corresponding to the clean configuration tested at Re $= 0.8 \times 10^5$; the curve begins from a 0° angle-of-attack and proceeds until reaching the maximum of 20°. The C_D value remains below 0.1 for the major part of the route, but it suffers from a sudden increase up to values above ≈ 0.15 when going beyond 10°: that's the stalling phenomenon, and the jump it produces may be better appreciated on the zoomed axes plotted below the main diagram and showing the $\alpha \in [0, 10]°$ region. After such a jump, C_D values below 0.1 are not regained even if the angle of attack descends from 10°, which is the configuration that triggers the stalling; in fact, it is necessary to decrease it until 8° before recovery occurs. Once the airfoil returns to its streamlined-body condition, the curve gets back to the 0° configuration, overlapping the C_D values obtained for the increasing part of the angular route and closing the loop. The phenomenon is similar when considering the turbulent case, although stalling occurs at a higher angle-of-attack because of the delaying effect of turbulence.

The second aspect has to do with the errorbars added to the data points. Those bars are calculated following the methodology outlined in the work of Zarketa-Astigarraga et al. [43], and it is not the purpose of the present study to discuss their derivation. Rather, the aim is to use those bars for establishing a criterion on the validity of the $C_D - \alpha$ curves. As the angle-of-attack undergoes a cyclic route, each angular configuration owns two different data points, one corresponding to the increasing part of the route and the other to the decreasing one. The zoomed regions at the left hand-side of the figure, drawn for the $\alpha = 5°$
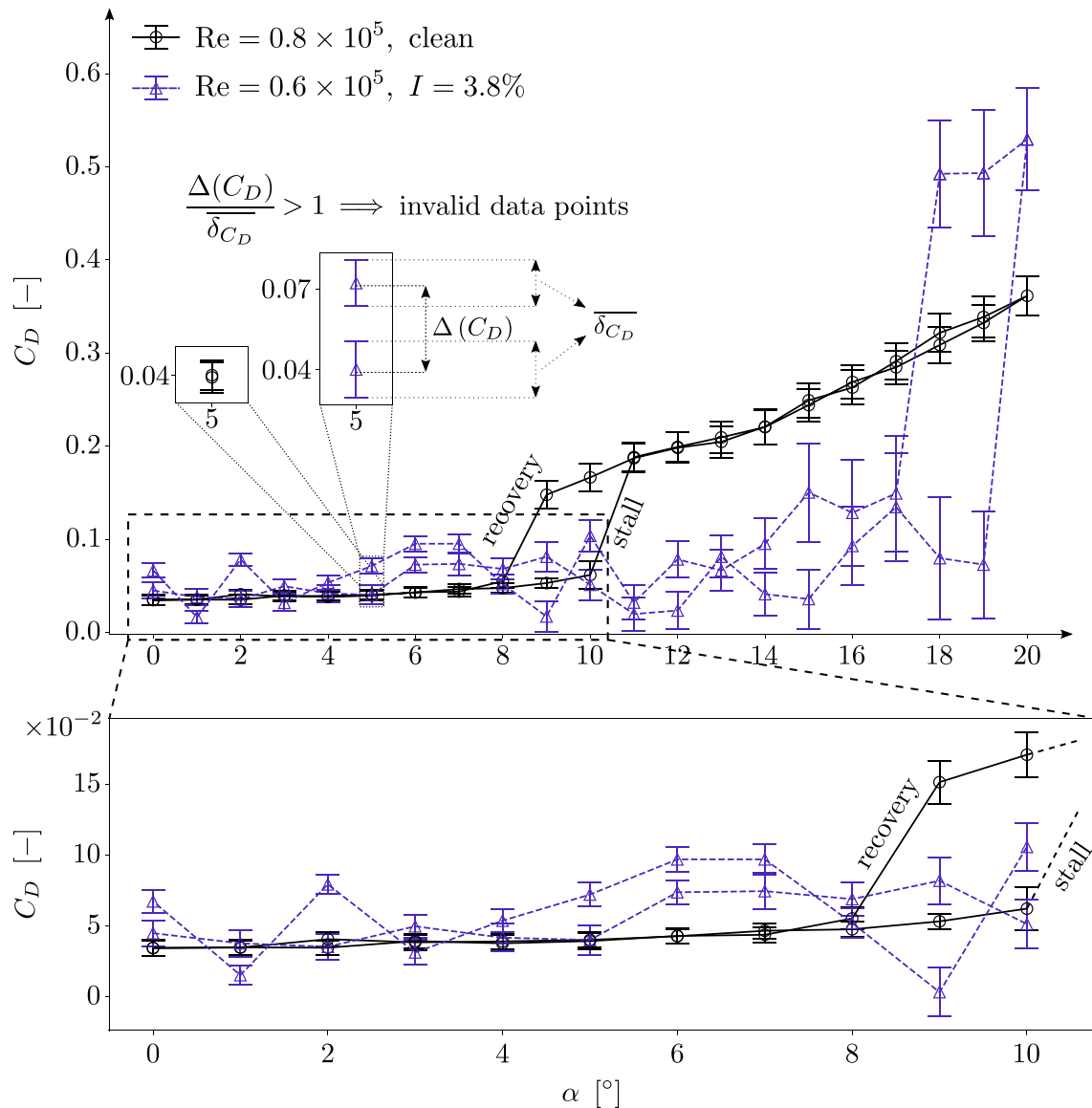
Fig. 9. representation of $C_D - \alpha$ curves and derivation of the acceptability criterion employed for discarding invalid turbulent configurations. The *x*-axis represents the angle of attack α, and the *y*-axis stands for the drag coefficient C_D. ⬡: $\text{Re} = 0.8 \times 10^5, I = 0.2\%$; △: $\text{Re} = 0.6 \times 10^5, I = 3.8\%$. The zoomed inset axes are intended to show the variables that enter the definition of the acceptability parameter, namely $\Delta(C_D)$ and $\overline{\delta_{C_D}}$, as well as the relative differences on such variables between the re.presented cases.

angular configuration, intend to show the pairing that occurs for each angular configuration, as well as the relative difference between the data points depending on the tested configuration. The zoomed diagram at the bottom of the figure also serves the purpose of showing the relative differences among the data-pairs of the plotted configurations at low α values.

Hence, a validity criterion for the $C_D - \alpha$ curves may be defined by the following parameter: consider the difference between the pair of data points that corresponds to each angular configuration, namely $\Delta(C_D)$, and compare it to the average of the uncertainty intervals of those points, i.e. $\overline{\delta_{C_D}}$. Such a ratio $\Delta(C_D)/\overline{\delta_{C_D}}$ may be interpreted in a straightforward manner: if it is larger than 1, it means that the pair of data points lie further apart from each other than their average uncertainty. Consequently, it is not possible to establish a well defined C_D value for such an angular configuration, and the $C_D - \alpha$ curve becomes inconsistent. In fact, as the curves represent the average of three different tests, a ratio $\Delta(C_D)/\overline{\delta_{C_D}} > 1$ means that individual tests are distinct beyond the threshold of experimental acceptability, and that

they do not converge to definite C_D values when they are averaged.

Having established a validity parameter for the $C_D - \alpha$ curves, Figs. 10–12 intend to show which of the configurations fulfill the newly defined acceptability criterion. Each of the three figures comprises two plots: the main one represents the $\Delta(C_D)/\overline{\delta_{C_D}}$ parameter against the angle-of-attack, and the subplot at the bottom stands for a portion of the $C_D - \alpha$ curve that is considered relevant for understanding the values acquired by the acceptability parameter. In case of Fig. 10, the plotted datasets correspond to the four clean configurations specified in Table 1; all values of $\Delta(C_D)/\overline{\delta_{C_D}}$, which are represented for $\alpha \in [0, 8]^\circ$, lie below the threshold line, and this indicates that the corresponding portions of the $C_D - \alpha$ curves are consistent, with the C_D values converging towards definite values. The bottom figure shows that such is the case, as the difference between the points of every data-pair plotted therein is less than the average of their respective uncertainty intervals. When the acceptability parameter lies closer to the threshold value, the corresponding data-pairs show a larger difference between them, as happens for the $\alpha \in [4, 6]^\circ$ configurations of the $\text{Re} = 0.6 \times 10^5$ case. The reason
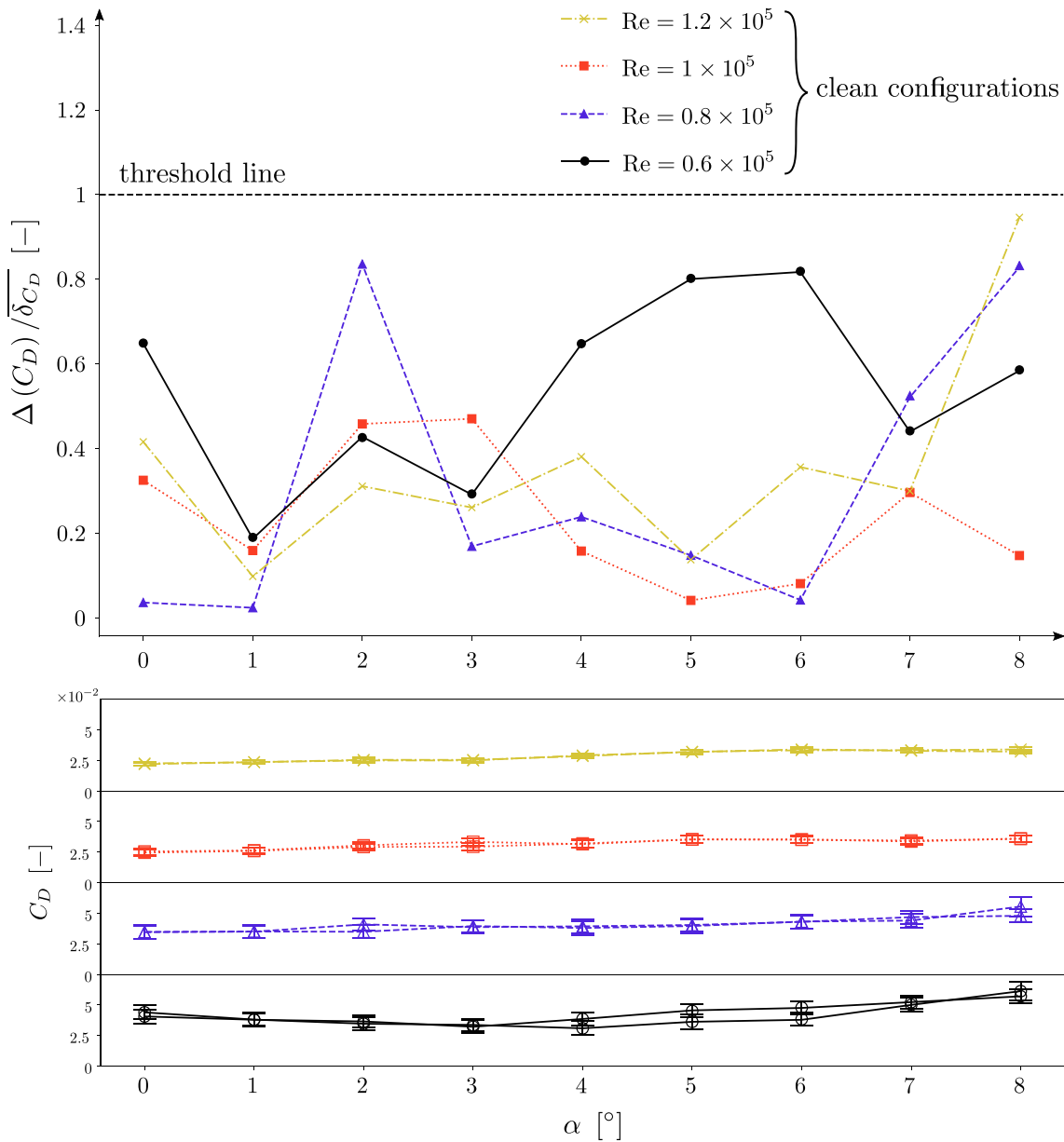
Fig. 10. angle-wise evolution of the acceptability criterion $\Delta(C_D)/\overline{\delta C_D}$ and corresponding portions of the $C_D - \alpha$ curves for the tested clean cases. ———●——— : Re = 0.6×10^5; – – –▲– – –: Re = 0.8×10^5; ·······■······· : Re = 1×10^5; —×—×— : Re = 1.2×10^5.

for limiting the range of α values shown in the plot has to do with the fact that the acceptability parameter is merely valid within the unstalled region of the airfoil; indeed, when the airfoil stalls two different phenomena take place. The first of them is the appearance of the already mentioned hysteresis cycle, which is clearly represented in Fig. 9. On the basis of the acceptability parameter, the data-pairs that constitute the hysteresis cycle are invalid; however, hysteresis itself is a genuine aerodynamic phenomenon, not a spurious effect coming from incorrect measurements, and hence the $\Delta(C_D)/\overline{\delta_{C_D}}$ parameter does not apply. The second phenomenon is the increase of the uncertainty intervals that takes place when stalling occurs, a feature that is straightforwardly explained by the uncertainty theory: as the intervals are directly dependent on the standard deviations of the measured magnitudes, and those deviations become noticeably larger under stalled conditions, the intervals also increase. Thus, although data-pairs in stalled conditions do not comply with the acceptability criterion, their validity comes at the cost of assuming a larger uncertainty on them, but there is no statistical reason for declaring them invalid altogether.

Fig. 11 represents the cases run at Re = 0.8×10^5 which, according to Table 1, comprise the three turbulent levels in addition to the clean configuration. The $C_D - \alpha$ subplot spans between $\alpha \in [0, 10]°$; including higher angles-of-attack is possible, because turbulent cases show a delayed stall as depicted on Fig. 9, and the angular range at which the acceptability parameter is well-defined extends accordingly (the datasets corresponding to the clean configuration are trimmed at $\alpha = 8°$, as it stalls at such an angle-of-attack). However, going to larger angles results in an increase of the C_D values, and the differences among the data-pairs become less discernible. The plotted datasets show that both the clean configuration and the one tested at $I = 3.8\%$ are valid altogether, with their respective acceptability parameters lying below the threshold line. Nevertheless, conflictive data-pairs begin to appear at lower turbulence intensities: the $I = 3\%$ case owns three points that fall marginally above $\Delta(C_D)/\overline{\delta_{C_D}} = 1$. Those points appear as non-overlapping data-pairs in the $C_D - \alpha$ curve, indicating inconsistent configurations at which the drag coefficient does not acquire a definite value according to the specified experimental uncertainty. The situation
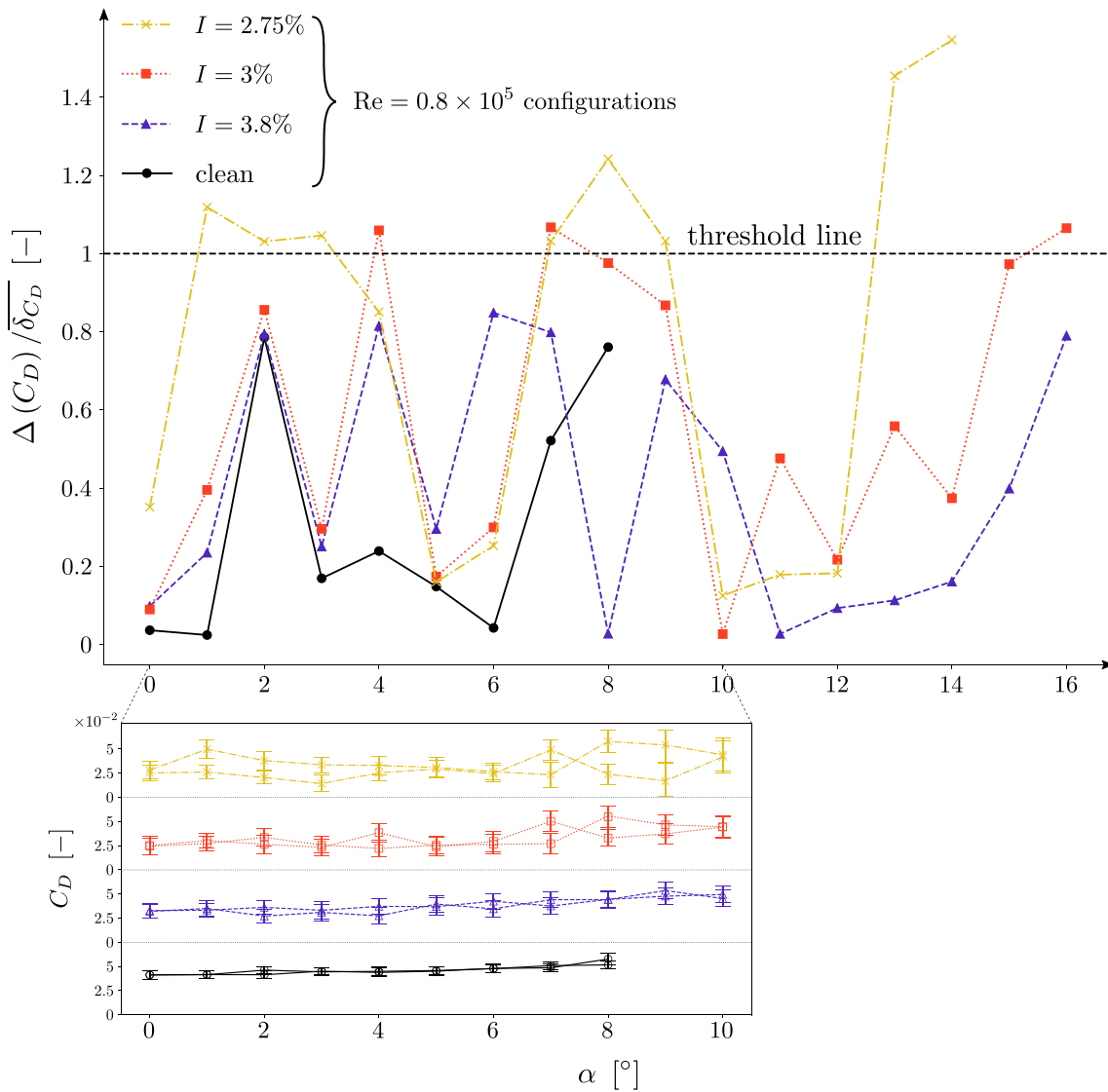
Fig. 11. angle-wise evolution of the acceptability criterion $\Delta(C_D)/\overline{\delta C_D}$ and corresponding portions of the $C_D - \alpha$ curves for both clean and turbulent cases run at Re $= 0.8 \times 10^5$ ——●——: clean; – – –▲– – –: turbulent at $I = 3.8\%$; ········■········: turbulent at $I = 3\%$; –·–×–·–: turbulent .at $I = 2.75\%$.

aggravates in case of the $I = 2.75\%$ configuration, for which the number of outliers is larger and their separation from the threshold line higher. The plotted $C_D - \alpha$ portion adopts the shape of two different curves in contrast to the single-line morphology of the clean configuration curve.

The analysis above leads to the conclusion that fulfilling the σ-based criterion is not sufficient for ensuring the applicabilty of the momentum-deficit technique to a flow configuration. Indeed, the $I = 3\%$ case is shown to comply with such a criterion in Fig. 6, but the resultant $C_D - \alpha$ curve owns a number of angles-of-attack for which the acceptability parameter lies above the threshold value. Thus, a *sk*-based criterion may be necessary for complementing the σ-based one.

Finally, Fig. 12 depicts four turbulent cases. The one tested at Re $= 0.8 \times 10^5$ and $I = 3.8\%$ has already been plotted in Fig. 11, and it merely serves comparative purposes herein. The remaining three have not been shown yet, and intend to exhaust the cases mentioned in Table 1. The first of such curves, namely the Re $= 0.6 \times 10^5$ and $I = 3.8\%$ configuration, is clearly invalid. Few of its $\Delta(C_D)/\overline{\delta C_D}$ values lie below the threshold line, and the corresponding $C_D - \alpha$ portion (also shown in Fig. 9) reflects such a fact with a highly inconsistent curve. This means that violating the σ-based criterion is a sufficient condition for turning a configuration invalid, as the mentioned case fulfills the isotropic condition according to Fig. 7, but fails to achieve standard deviation values

below 0.05 as shown in Fig. 6.

The other two configurations, i.e. the Re $= \{1, 1.2\} \times 10^5$ ones tested at $I = 2.75\%$, corroborate the conclusion drawn from Fig. 11. These cases fulfill the σ-based criterion, but stand at the final anisotropic region shown in Fig. 7, where both the *sk* and *ku* parameters acquire large values, indicating the end of quasi-HIT conditions. Formally, both of these cases represent invalid turbulent configurations, as they show a number of data points lying above the threshold line. However, the effect of the Reynolds number becomes evident, as increasing it seems to induce a lowering on the number of data points that are invalid, as well as taking those points closer to the threshold line. Nevertheless, and due to the technical limitations of the current set-up (refer to Section 3.4), checking whether larger Reynolds numbers produce valid $C_D - \alpha$ curves at $I = 2.75\%$ has not been possible. With all, the hypothesis established at the end of the turbulence characterization section has been corroborated: in addition to owning low standard deviation values, it is necessary that the tested configurations lie within the isotropic range of the turbulent flowfield.

As a synthesis, Fig. 13 provides a validity map drawn upon the Re $-I$ space. There is a narrow stripe of valid cases corresponding to the clean configurations. The region above shows three distinct zones: the red-coloured one stands for the invalid configurations that violate either
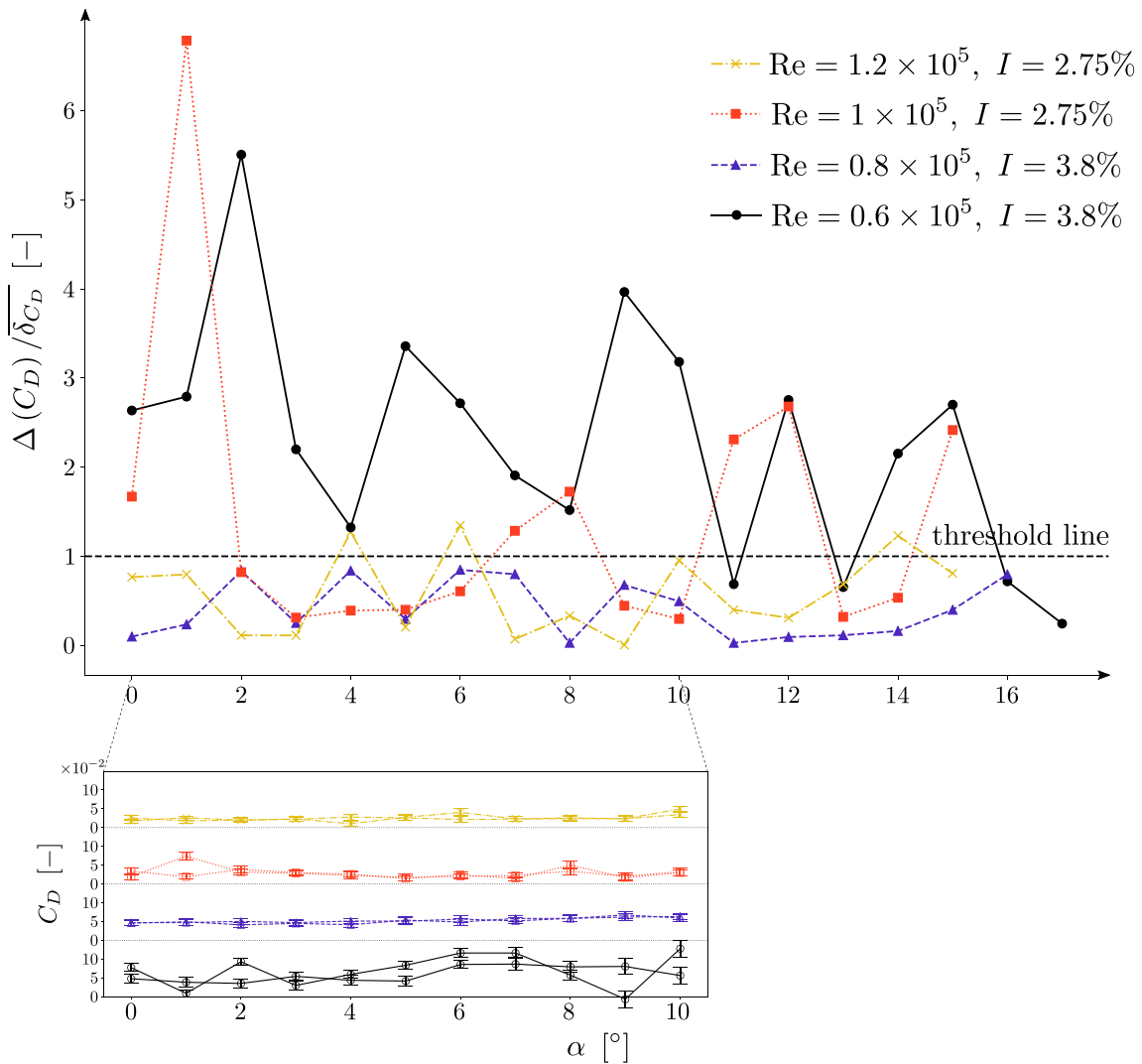
Fig. 12. angle-wise evolution of the acceptability criterion $\Delta(C_D)/\overline{\delta_{C_D}}$ and corresponding portions of the $C_D - \alpha$ curves for a set of turbulent cases. ●——: turbulent at Re $= 0.6 \times 10^5$ and $I = 3.8\%$; – – ▲ – –: turbulent at Re $= 0.8 \times 10^5$ and $I = 3.8\%$; ·····■·····: turbulent at Re $= 1 \times 10^5$ and $I = 2.75\%$; – ×– ·–: turbulent at Re $= 1.2 \times 10^5$ a.nd $I = 2.75\%$.

the σ- or the *sk*-based criteria. The invalid configurations corresponding to the lowest Reynolds number cases, namely Re $= \{0.6, 0.8\} \times 10^5$, do not comply with the σ-based criterion, whereas the ones run at the largest numbers (Re $= \{1, 1.2\} \times 10^5$) lie outside the isotropic region in spite of showing acceptable σ values.

As opposed, the green-coloured zone represents the valid configurations, or those for which the mentioned two criteria are met. The yellow-coloured stripe standing between the mentioned zones corresponds to an intermediate region. The cases that lie within such a region show certain angles-of-attack for which the validity parameter $\Delta(C_D)/\overline{\delta_{C_D}}$ lies above the threshold line. However, such invalid configurations are few in number and their respective validity parameters do not exceed the threshold value by large. As an illustrative example, consider the evolution of the Re $= 1.2 \times 10^5, I = 2.75\%$ case in Fig. 12: when compared to other invalid configurations, such a case lies close to being an acceptable candidate for undertaking momentum-deficit-based measurements. If the validity criterion defined herein is to be considered as a rigorous condition that the measured data must obey, then it is sensible to assert that the example curve we are alluding to represents an invalid configuration; if, otherwise, such a condition is relaxed and it is left to the experimentalist to decide whether those quasi-acceptable cases represent genuine $C_D - \alpha$ curves, then it makes sense to draw an

intermediate region between the valid and invalid zones.

Additionally, such an intermediate zone shows two distinct slopes depending on the considered Reynolds number. There is an initial region for which the evolution shows a highly negative trend, and corresponds to the Reynolds numbers that correlate with the turbulence cases not complying with the σ-based criterion. Beyond Re $= 0.8 \times 10^5$ the slope becomes milder and, if the map were to continue for larger Reynold numbers, the intermediate zone would asymptotically approach the valid region of clean configurations. Thus, it seems that there would be no invalid configurations for high testing velocities, for which the validity regions of clean and turbulent cases would merge.

With all, the validity map conveys a configuration-dependent picture, in the sense that a different experimental set-up, as well as distinct measurement techniques, are liable to yield a different map. More importantly, Section 3.4 mentions that the analysis is carried out on the basis of a particular confidence level, which is a parameter that the experimentalist can choose. The choice in this study has been to consider a level of 95%, but it may be reasonable to lower it due to the inherent dynamics of transitional flows, in which case the map will also vary. However, the procedure outlined herein has been designed in an application-agnostic manner, meaning that any research team willing to undertake momentum-deficit-based C_D measurements in turbulent
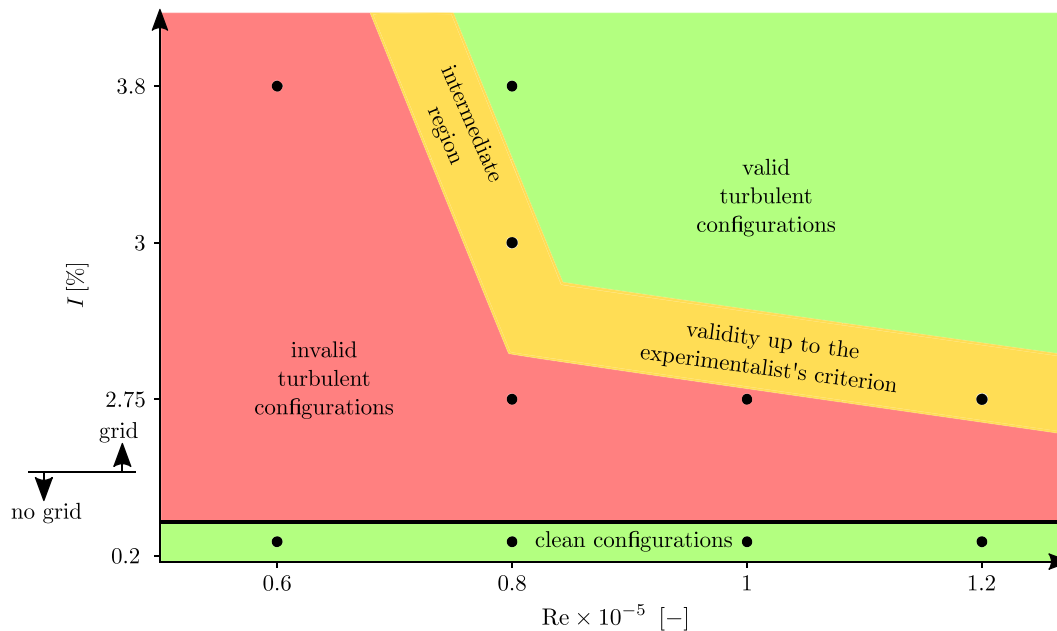
Fig. 13. validity map showing the feasibility of performing momentum-deficit-based C_D measurements depending on the testing Reynolds number (*x*-axis) and turbulent intensity (*y*-axis). The points ● represent tested configurations.

configurations can apply it to its own wind tunnel configuration and equipment.

5. Conclusions

Extending the possibility of performing momentum-deficit-based C_D measurements to turbulent configurations is a major step in the design process of airfoils, mainly due to the fact that real world applications such as wind turbines or drones are likely to face those flow conditions. The current study has explored such a possibility by undertaking a twofold analysis on the data coming from wake-rake measurements that correspond to flow configurations with varying Reynolds numbers and turbulence intensity levels.

The first part of the analysis focuses on characterizing the turbulent flowfield downstream a grid by means of certain statistical parameters of the velocity fluctuations, namely the standard deviation, the skewness and the kurtosis. The result of such an analysis is the observation that different acceptability criteria may be required for ensuring the feasibility of momentum-deficit measurements. The relevance of those criteria are checked in the second part of the analysis by obtaining $C_D - \alpha$ curves under conditions that comply with all, some or none of the criteria derived from the turbulence characterization process, and determining which of those curves are acceptable on the basis of a newly defined validity parameter. The major findings and concluding remarks are summarized below:

- Two conditions must be fulfilled for determining the wind tunnel region within which it is acceptable to perform C_D measurements upon turbulent conditions. The first condition is that the standard deviation of the velocity fluctuation must stand below a threshold value of $\sigma = 0.05$ (σ-based condition), ensuring that the measurements are acceptable in terms of experimental uncertainty. The second condition states that the skewness parameter has to show a constant, close-to-zero value (*sk*-based condition), guaranteeing that the flow is isotropic.
- The turbulent flowfield is divided into three distinct regions according to the general evolutions of the statistical parameters: an initial non-homogeneous, anisotropic zone of rapid σ and *sk* decay; an intermediate region of quasi-HIT conditions where measurements

are possible; and a final decay region where the flow ceases to be isotropic.
- Violating the σ-based criterion is sufficient for making the momentum-deficit-technique inapplicable to a given turbulent configuration. Nevertheless, fulfilling it is just a necessary condition for undertaking C_D measurements.
- An acceptability parameter, namely $\Delta(C_D)/\overline{\delta_{C_D}}$, is defined for checking the validity of momentum-deficit-based measurements in unstalled conditions. When lying above 1, it indicates that the C_D measured at a given angle-of-attack does not converge to definite values, turning the $C_D - \alpha$ curve inconsistent.
- An analysis based on the acceptability parameter corroborates that the σ-based criterion is necessary, but not sufficient, for determining the validity of momentum-deficit-based C_D measurments. It is required to complement such a condition with a *sk*-based criterion for ensuring flow isotropy and consistent $C_D - \alpha$ curves.
- The validity map drawn upon the $\mathrm{Re} - I$ space, which provides a summarized view of the valid turbulent configurations, is application-dependent. A different experimental set-up or measurement equipment will probably yield a modified version of the chart, and the results obtained herein are to be interpreted as case-specific. However, the procedure itself is designed in an application-agnostic manner, meaning that any research team willing to undertake C_D measurements in turbulent configurations can adapt it to its own particular set-up.

Declaration of Competing Interest

The authors declare that they have no known competing financial interests or personal relationships that could have appeared to influence the work reported in this paper.

Project FETRAFLU [2018-CIEN-000101–01].

References

[1] José Meseguer-Ruiz and Ángel Sanz-Andrés. Procedimientos para determinar numéricamente la resistencia. In Aerodinámica Básica, chapter 9.2, pages 262–264. Garceta Grupo Editorial, 2 edition, 2012.

[2] Force and Moment Measurement. In Cameron Tropea, John Foss, and Alexander Yarin, editors, Springer Handbook of Experimental Fluid Mechanics, chapter 8, pages 563–616. Springer, 1 edition, 2007.

[3] M.A. González, J.M. Ezquerro, V. Lapuerta, A. Laverón, J. Rodríguez, Components of a Wind Tunnel Balance: Design and Calibration. Wind Tunnels and Experimental, Fluid Dyn. Res. (2011) 1–20.

[4] G. Ananda, Aerodynamic performance of low-to-moderate aspect ratio wings at low Reynolds numbers, PhD thesis, University of Illinois at Urbana-Champaign, 2012.

[5] G. Ananda, P. Sukumar, and M. Selig. Measured Aerodynamic Characteristics of Wings at Low Reynolds Numbers. PhD thesis, 2015.

[6] L.M.M. Boermans, Research on sailplane aerodynamics at Delft University of Technology, Recent and present developments. Technical Soaring 30 (1–2) (2006) 1–25.

[7] S.L. Yang, G.R. Spedding, Spanwise variation in circulation and drag of wings at moderate reynolds number, Journal of Aircraft 50 (3) (2013) 791–797.

[8] Selig, Donovan, and Fraser. Airfoils at Low Speeds. Virginia Beach, VI, U.S.A, 1989.

[9] M.S. Selig, New Airfoils for Small Horizontal Axis Wind Turbines, ASME Journal of Solar Energy Engineering 120 (1998) 1–7.

[10] Philippe Giguère, Michael S Selig, Aerodynamic effects of leading-edge tape on aerofoils at low Reynolds numbers, Wind Energy 2 (3) (1999) 125–136.

[11] Michael S. Selig and Bryan D. McGrahanan. Wind Tunnel Aerodynamic Tests of Six Airfoils for Use on Small Wind Turbines. Technical report, National Renewable Energy Laboratory (NREL), Golden, CO, U.S.A, 2004.

[12] Harold Youngren, Chris Kroninger, Ming Chang, and Steve Jameson. Low reynolds number testing of the AG38 airfoil for the SAMARAI nano air vehicle. In 46th AIAA Aerospace Sciences Meeting and Exhibit, number January, pages 1–31, 2008.

[13] Xuanshi Meng, Hu. Haiyang, Xu. Yan, Feng Liu, Shijun Luo, Lift improvements using duty-cycled plasma actuation at low Reynolds numbers, Aerosp. Sci. Technol. 72 (2018) 123–133.

[14] D. Holst, B. Church, G. Pechlivanoglou, E. Tüzüner, J. Saverin, C.N. Nayeri, C. O. Paschereit, Experimental analysis of a NACA 0021 airfoil section through 180-deg angle of attack at low Reynolds numbers for use in wind turbine analysis, J. Eng. Gas Turbines Power 141 (4) (2019).

[15] A.D. Young. Boundary Layers. AIAA education series. American Institute of Aeronautics and Astronautics, 1989.

[16] S. Watkins, S. Ravi, B. Loxton, The effect of turbulence on the aerodynamics of low Reynolds number wings, Engineering Letters 18 (3) (2010).

[17] S. Watkins, M. Thompson, B. Loxton, M. Abdulrahim, On low altitude flight through the atmospheric boundary layer, International Journal of Micro Air Vehicles 2 (2) (2010) 55–68.

[18] M. Thompson, S. Watkins, C. White, J. Holmes, Span-wise wind fluctuations in open terrain as applicable to small flying craft, Aeronaut. J. 115 (1173) (2011) 693–701.

[19] Simon Watkins, Alex Fisher, Abdulghani Mohamed, Matthew Marino, Mark Thompson, Reece Clothier, and Sridhar Ravi. The Turbulent Flight Environment Close to the Ground and Its Effects on Fixed and Flapping Wings at Low Reynolds Number. 5th European Conference for Aerospace Sciences (EUCASS), (July): 1–10, 2013.

[20] P.E. Roach, The generation of nearly isotropic turbulence by means of grids, Int. J. Heat Fluid Flow 8 (2) (1987) 82–92.

[21] P.A. Krogstad, P.A. Davidson, Is grid turbulence Saffman turbulence? J. Fluid Mech. 642 (2010) 373–394.

[22] K E Swalwell, J Sheridan, and W H Melbourne. The Effect of Turbulence Intensity on Stall of the NACA 0021 Aerofoil. In 14th Australasian Fluid Mechanics Conference, pages 941–944, Adelaide, Australia, 2001. Adelaide University.

[23] Ph Devinant, T. Laverne, J. Hureau, Experimental study of wind-turbine airfoil aerodynamics in high turbulence, J. Wind Eng. Ind. Aerodyn. 90 (2002) 689–707.

[24] Luca Petricca, Per Ohlckers, Christopher Grinde, Micro- and nano-air vehicles: State of the art, International Journal of Aerospace Engineering 1–17 (2011) 2011.

[25] Ivan Torrano, Low speed wind tunnel design, setup, validation and testing of airfoils in turbulent in ow conditions, PhD thesis, Mondragon Goi Eskola Politeknikoa, 2016.

[26] G.K. Batchelor, The theory of homogeneous turbulence, 1 ed., Cambridge University Press, 1953.

[27] Uriel Frisch. Two experimental laws of fully developed turbulence. In Turbulence: the legacy of A.N. Kolmogorov, chapter 5, pages 57–71. Cambridge University Press, 1 edition, 1995.

[28] José Olarrea-Busto and Marta Cordero-Gracia. Variable Aleatoria. In Estadística: 45 Problemas útiles, chapter 3, pages 65–104. García-Maroto Editores, 1 edition, 2007.

[29] Geneviève Comte-bellott, Stanley Corrsin, The use of a contraction to improve the isotropy of grid-generated turbulence, J. Fluid Mech. 25 (1966) 657–682.

[30] S. Mohamed Mohsen, John C. LaRue, The decay power law in grid-generated turbulence, J. Fluid Mech. 219 (1990) 195–214.

[31] A. Betz. A method for the direct determination of wing-section drag. Technical report, Washington, WA, U.S.A, 1925.

[32] B.M. Jones. The Measurement of Profile Dra by the Pitot-traverse Method. Aeronautical Research Committee. Reports and memoranda. H.M. Stationery Office, 1936.

[33] William Bollay, Determination of Profile Drag from Measurements in the Wake of a Body, Journal of the Aeronautical Sciences (1938) 245–248.

[34] On the decomposition of drag components from wake flow measurements. In 35th Aerospace Sciences Meeting and Exhibit, number January, Reno, NV, U.S.A, 1997. American Institute for Aeronautics and Astronautics (AIAA).

[35] A. Picard, R.S. Davis, M. Gläser, K. Fujii, Revised formula for the density of moist air (CIPM-2007), Metrologia 45 (2) (2008) 149–155.

[36] Allan J Zuckerwar, Roger W Meredith, Low-frequency absorption of sound in air, Journal of Acoustical Society of America 78 (September) (1985) 946–955.

[37] Aditya Vaidyanathan, David Kingman, Theresa Kurth, When do endplates work?, in: 52nd Aerospace Sciences Meeting, 2014, pp. 1–11.

[38] Arkady Tsinober. An informal conceptual introducion to turbulence, volume 53. Springer, 1 edition, 2009.

[39] Ivan Torrano, Mustafa Tutar, Manex Martinez-Agirre, Anthony Rouquier, Nicolas Mordant, Mickael Bourgoin, Comparison of experimental and rans-based numerical studies of the decay of grid-generated turbulence, J. Fluids Eng. 137 (6) (2015) 06.

[40] Labview software main page. https://www.ni.com/en-us/shop/labview.html.

[41] L. Djenidi, Md. Kamruzzaman, R.A. Antonia, Power-law exponent in the transition period of decay in grid turbulence, J. Fluid Mech. 779 (2015) 544–555.

[42] Nicolas Mordant, Experimental high Reynolds number turbulence with an active grid Experimental high Reynolds number turbulence with an active grid, Am. J. Phys. 76 (2008) 1092–1098.

[43] Ander Zarketa-Astigarraga, Alain Martin-Mayor, Manex Martinez-Agirre, Experimental uncertainty decompositions of aerodynamic coefficients affected by operative condition variations, Measurement 165 (C) (2020) 1–14.

[44] J.S. Kline, F.A. McClintock, Uncertainties in single-sample experiments, Mechanical Engineering (1953) 3–8.

[45] Justin Winslow, Hikaru Otsuka, Bharath Govindarajan, Inderjit Chopra, Basic understanding of airfoil characteristics at low Reynolds numbers (104–105), Journal of Aircraft 55 (3) (2018) 1050–1061.

[46] M. Ol, B. McAuliffe, E. Hanff, U. Scholz, and C. Kähler. Comparison of Laminar Separation Bubble Measurements on a Low Reynolds Number Airfoil in Three Facilities. In American Institute for Aeronautics and Astronautics (AIAA), editor, 35th AIAA Fluid Dynamics Conference and Exhibit, pages 1–11, Toronto, Ontario, Canada, 2005. American Institute for Aeronautics and Astronautics (AIAA).

[47] James J Guglielmo, Michael S. Selig, Large spanwise variations in profile drag for airfoils at low Reynolds numbers, 13th Applied Aerodynamics Conference 33 (1995) 174–184.

[48] R.J. Moffat, Contributions to the Theory of Single-Sample Uncertainty Analysis, J. Fluids Eng. 104 (1982).

[49] R.B. Abernethy, R.P. Benedict, R.B. Dowdell, ASME Measurement Uncertainty, J. Fluids Eng. 107 (1985) 161–164.

[50] Robert J. Moffat, Describing the Uncertainties in Experimental Results, Exp. Thermal Fluid Sci. 1 (1988) 3–17.